



Elastic thin shells with large axisymmetric imperfection: from bifurcation to snap-through buckling

Chuan Qiao, Lu Liu, Damiano Pasini*

Department of Mechanical Engineering, McGill University, Montreal, Quebec H3A 0C3, Canada



ARTICLE INFO

Article history:

Received 13 December 2019

Revised 4 March 2020

Accepted 3 April 2020

Available online 29 April 2020

Keywords:

Spherical shells

Snap-through

Buckling

Geometric imperfections

Soft metamaterials

ABSTRACT

Elastic thin shells are well-known for their highly unstable post-buckling, a response that exhausts their pressure bearing capacity and leads to catastrophic collapse. This paper examines elastic thin shells with a large axisymmetric imperfection that can escape the classical bifurcation of perfect spherical shells. We employ a shell theory formulation with exact expressions of the middle surface strains, curvature changes, and live pressure along with validating experiments and numerical simulations. The results show that a large axisymmetric imperfection in the form of a circular arc can induce snap-through buckling followed by a stable post-buckling that offers increasing resistance to pressure over a large change in volume. In addition, a sensitivity analysis on the role of defect geometry and shell radius to thickness ratio reveals the emergence of four buckling modes. For small imperfections, bifurcation buckling (mode 1) is dominant and resembles the typical dimple-like mode of perfect spherical shells. For larger imperfections, the shell attains the maximum pressure at the snap-through buckling where strain localization appears either within the imperfection (mode 2) or just below (mode 3). In the fourth mode, snap-through buckling precedes the attainment of the maximum pressure following a post-buckling path characterized by a large change of volume that makes the shell harder and stronger. These findings show that harnessing defect geometry and shell radius to thickness ratio can be effective in programming the post-buckling characteristics and transition between buckling modes, thus offering potential routes for the design of soft metamaterials with application to soft robotics and other sectors.

© 2020 Elsevier Ltd. All rights reserved.

1. Introduction

Spherical thin shells are ubiquitous in nature from the cell wall of baker's yeast (Arfsten et al., 2010), virus shells (Vaziri and Mahadevan, 2008), to pollen grains (Katifori et al., 2010), and coconut shells (Nguyen et al., 2016). They are also widespread in engineering across the spectrum of length scale, from microcapsules for drug delivery (Jose et al., 2014), to pressure vessels (Blachut and Magnucki, 2008), and underwater pressure hulls (Pan et al., 2010, 2012). The mechanics of spherical thin shells, in particular their nonlinear buckling behaviour, has been extensively studied over the past decades. One of the main findings is that under a uniformly applied external pressure, spherical thin shells exhibit a highly unstable post-buckling response characterized by a sudden drop of load bearing capacity and a strong sensitivity to im-

* Corresponding author.

E-mail address: damiano.pasini@mcgill.ca (D. Pasini).

perfections. In his seminal work, [Zoelly \(1915\)](#) was the first to study defect-free shells through classical linear theory and to derive expressions for the theoretical pressure at which buckling occurs. These predictions offer a buckling load baseline that substantially departs from experimental measures, which typically reach only 1/5 of their theoretical values. This discrepancy is conveniently gauged by the knockdown factor, the ratio of the experimentally measured buckling pressure over its theoretical counterpart, which is commonly used for shell design, and for as-built shells it has a wide span from 0.05 to 1.1 ([Carlson et al., 1967](#); [Evkin and Lykhachova, 2017](#); [Homewood et al., 1961](#); [Kaplan and Fung, 1954](#); [Krenzke and Kiernan, 1963](#); [NASA, 1969](#); [Seaman, 1962](#); [Tsien, 1942](#); [Wagner et al., 2018](#)).

The causes for the low tested values of buckling pressure have been extensively studied for spherical shells ([Bushnell, 2014](#); [Hutchinson and Koiter, 1970](#); [Thompson and Heijden, 2014](#)). Among the first were [von Kármán and Tsien \(1939, 1941\)](#), who proposed the notion of a “lower buckling pressure” to indicate the minimum load necessary to keep the shell in the buckled shape. This pressure was arguably supposed to be independent of the load arrangement and the initial imperfections of the shell. Only thereafter, the issue was elucidated by [Koiter \(1945\)](#) with his theory of elastic stability under conservative loadings, corroborated later via experiments ([Carlson et al., 1967](#)). From this theory the critical role of geometric imperfections has been unveiled with results showing the high sensitivity of both the critical load and the initial post-buckling behavior to geometric defects, even when these are very small in amplitude.

Geometric imperfections induced by fabrication are typically distributed randomly in a real shell. Since their geometry and size are not always easily quantifiable, a practical approach to obtain at most a qualitative account of the real shell response is to intentionally introduce as-designed imperfections in their ideal geometry. This approach has been widely adopted in the literature of thin shells. For example, [Koga and Hoff \(1969\)](#) were among the first to study the role of imperfections introduced in the form of increased-radius and dimple geometries. Their investigation shed light into the role of a number of geometric defects including defect amplitude, angular width and radius to thickness ratio of the shell. Asymmetric pie-shaped imperfections in spherical caps were also studied ([Kao, 1972](#)) through a strain-displacement formulation similar to that of Donnell’s cylindrical shell theory ([Donnell, 1934](#); [Donnell and Wan, 1950](#)). The computational results shows a buckling pressure lower than those previously found ([Kao and Perrone, 1971](#)). Imperfections in the form of Legendre polynomials ([Fan, 1989](#)) were also later studied with the goal of assessing the post-buckling behavior and the sensitivity to defect size. More recently Blachut ([Blachut, 2015, 2016](#); [Blachut and Galletly, 1993](#)) performed a series of studies on the buckling of geometrically imperfect domes embedding a set of defects defined by Legendre polynomials, localized flattening, eigenmode imperfections, local inward dimple of arbitrary shape, and force-induced inward dimple. A direct relationship was established by [Lee et al. \(2016b\)](#) between the experimental buckling pressure and a set of imperfections with varying geometry. The results reveal that defect sensitivity diminishes with the amplitude of the imperfection reaching a threshold value (larger than the shell thickness), above which the knockdown factor of the buckling pressure levels out on a plateau.

Most of the existing works on defect sensitivity of shell buckling have so far studied the post buckling regime, i.e. a monotonic drop of pressure which rapidly exhausts the shell resistance until sudden collapse occurs. This phenomenon deprives shell functionality and has two main features. First, prior to bifurcation, the shell deformation, in particular the displacement of the pole, is tiny compared to the shell radius, thereby yielding almost no change in volume ([Hutchinson, 2016](#)). Second, under a given pressure the shell is unstable for the entire post-buckling regime ([Hutchinson, 2016](#)), showing the inability to resist any increase in pressure and spontaneous marching towards full eversion.

In this work, we examine an elastic thin shell shaped with a large axisymmetric imperfection that can bypass the catastrophic collapse typically observed in hemispherical shells under external pressure. While previous works aiming at tuning the post-buckling characteristics of thin shells examine certain types of imperfections, such as soft spots ([Paulose and Nelson, 2013](#)) and creases ([Bende et al., 2015](#)), here we explore an alternative route. More specifically, we introduce a parametric set of geometric imperfections ([Section 2](#)) that can alter the post-buckling response from a pure monotonic fall of pressure to a stable response with pressure resistance gained through large volumetric deformation. Experiments on proof-of-concepts shells ([Section 3.1](#)), theoretical analysis ([Section 3.2](#)), and finite element method (FEM) simulations ([Section 3.3](#)) are presented to show a buckling response over a large volume change (above 20% the initial volume), a behaviour previously unobserved in the literature of hemispherical thin shells. Finally, a sensitivity study ([Section 4](#)) unveils a direct relation between shell response, defect characteristics and shell geometry, which altogether can be tuned to render three distinct snap-through modes besides bifurcation buckling, which can be exploited for the design of soft metamaterials for soft robotics, mechanism-based structures and smart actuators.

2. Shell geometry with large geometric imperfection

We consider a hemispherical thin shell ([Fig. 1](#)) with a large geometric imperfection in the form of an axisymmetric circular-arc indentation that can vary in amplitude, angular width and location. The cross-section of the shell is defined by the radius R and thickness t , defining its slenderness, R/t . The large imperfection traces a circular arc with center O_2 and extent defined by h/l , i.e. the amplitude h to width l ratio, and the angular width θ_w . We examine the cases where the imperfection can vary in angular width θ_w ([Fig. 1c](#)), in position through the meridional angle θ_m ([Fig. 1d](#)), defining the position of its center O_2 , and in amplitude h/l from 0 and 0.5 ([Fig. 1e](#)), the former describing the case of an arc collapsed to a line segment, and the latter being a defect in the form of a semicircle. The imperfection is also assumed to lie between the equator and the upper pole of the semi circumference ([Fig. 1e](#)), hence satisfying the constraint on the meridional angle

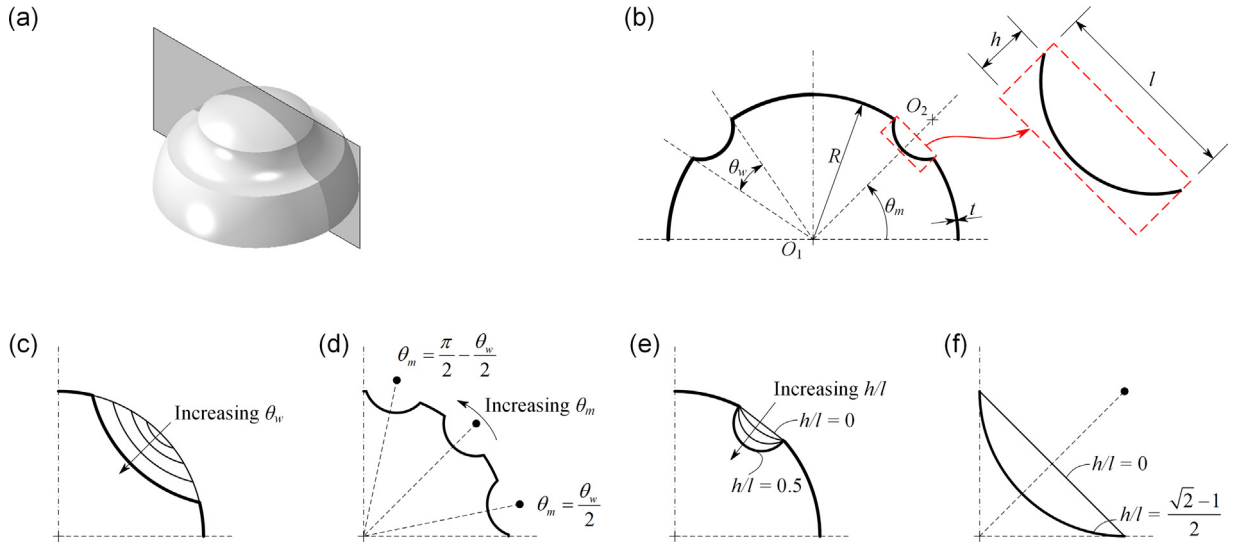


Fig. 1. (a) Three-dimensional view with an intersecting symmetry plane of a shell with a large geometric imperfection. (b) Shell cross-section on the intersecting plane, with shell geometry described by radius R , radius to thickness ratio R/t , imperfection angular width θ_w , imperfection amplitude h/l , and meridional angle θ_m . Effect of varying defect size and location: (c) increase in defect width through change of θ_w , (d) defect center location through variation of meridional angle, θ_m , (e) defect amplitude for increasing h/l . (f) Special cases: $h/l=0$ yields a linear profile generating a conical shell, $h/l=(\sqrt{2}-1)/2$ gives a concave profile, i.e. an arc generatrix for a surface of revolution that departs from the spherical and conical geometry.



Fig. 2. Fabrication steps. (a) 3D printed hemispherical shape mold with axisymmetric circular-arc indentation. A groove at the bottom of the mold is introduced to collect excessive polymer deposition. (b) VPS liquid poured onto the mold surface. (c) Stabilized shell sample removed from the mold.

θ_m and the angular width θ_w :

$$\frac{\theta_w}{2} < \theta_m < \frac{\pi}{2} - \frac{\theta_w}{2} \quad (1)$$

Fig. 1f shows two special cases for extremely large imperfections with width $\theta_w = \pi/2$ and meridional angle $\theta_m = \pi/4$. The hemispherical shell degenerates into either a cone for amplitude $h/l=0$, or for $h/l=(\sqrt{2}-1)/2$ into a surface of revolution obtained by rotating the generatrix, a concave arc, around the vertical axis.

3. Methods

3.1. Experiment

3.1.1. Manufacturing of elastic thin shells and shell geometry assessment

Fig. 2 shows the basic steps of the manufacturing process adapted from the literature (Lee et al., 2016a,b) to build shell samples with thin hemispherical smooth geometry. We first used fused deposition modeling (FDM) to 3D print a 1 mm-thick mold (Fig. 2a) made of Onyx filament, and then poured a silicone-based elastomer solution onto its surface to form a thin shell. Table 1 lists the nominal surface geometry of the as-designed mold, which slightly differs from that of the as-built mold. Measures of the radius made with a digital caliper at the equator of the hemisphere provided $R = 24.72$ mm, a value 1% below from the nominal one.

For the shell material, we chose Vinylpolysiloxane (VPS, Elite Double 32, Zhermark), whose Young's modulus and Poisson's ratio (Table 2) were previously measured (Pezzulla et al., 2015). After mixing catalyst and base with equal volume

Table 1

Nominal geometry of the 3D printed mold.

$R(\text{mm})$	$\theta_w(^{\circ})$	h/l	$\theta_m(^{\circ})$
24.86	25.2	0.2	43.3

Table 2

Measured elastic properties of VPS (Pezzulla et al., 2015) and computed coefficients of the neo-Hookean model.

Linear elastic model		Neo-Hookean model	
E (MPa)	ν	C_{10} (MPa)	D_1 (MPa ⁻¹)
0.96	0.5	0.16	0

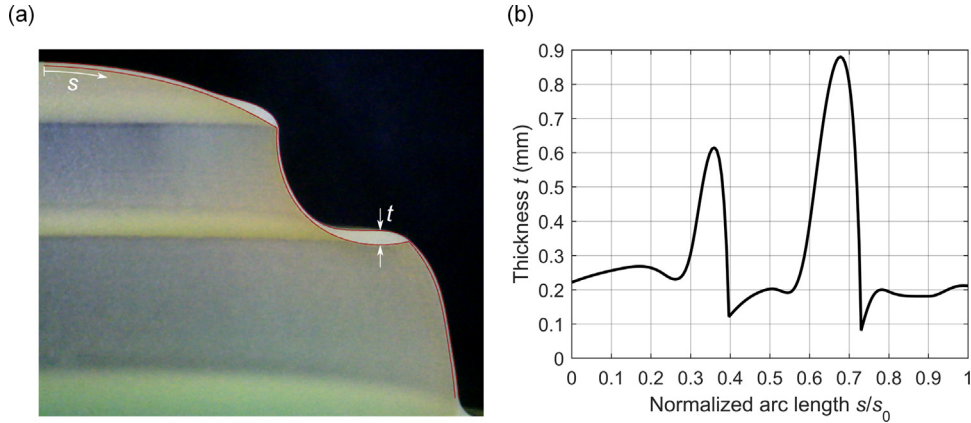


Fig. 3. (a) Photograph of half cross-section of a representative sample cut along the symmetry plane. Red curves trace lower and upper boundaries of shell surfaces. (b) Shell thickness, t , variation traced from (a) and plotted against the normalized arc length s from pole to equator, where s_0 is the total arc length from the upper pole to the equator. The thickness profile is relatively uniform at about 0.2 mm, with peaks of $t = 0.61\text{mm}$ at $s/s_0 = 0.36$ and $t = 0.88\text{mm}$ at $s/s_0 = 0.68$.

fraction, VPS was poured on the surface of the 3d printed mold (Fig. 2b). During the pouring process, excessive liquid accumulated at the bottom of the mold and formed a band of 2 mm thickness, which acted as clamp at the low boundary of the hemispherical shell. After the complete VPS stabilization at room temperature, the thin shell was peeled off the mold (Fig. 2c).

The protocol above was followed to manufacture eight samples of identical geometry, and Fig. 3a shows the cross-section of a representative along the symmetry plane. From a detailed assessment of the shell thickness across the entire shell domain (Fig. 2c), we observe thickness uniformity along the circumferential direction only. In contrast, along the meridional direction major divergences appear. This is evident in Fig. 3a, where the inner and outer profiles (red) are fitted with two splines (NURBS). From a top to bottom inspection, we notice the VPS pouring onto the mold surface resulted in two sets of local non-uniform thickening: one above the large imperfection and the other of larger amplitude at its bottom. The distance between the inner and outer profiles (red curve in Fig. 3a) were assessed at 196 points along the arc length direction, and the thickness profile was adjusted by comparing the maximum thickness obtained from the optical image to the measurement from the digital caliper. Fig. 3b plots the scaled thickness profile as a function of the normalized arc length from the upper pole to the equator. The maximum thickness of the eight samples is $t = 0.88 \pm 0.03\text{mm}$. The thickness profile is relatively uniform with $t = 0.20\text{mm}$ and minor fluctuations of 0.07 mm along the normalized arc length, except for peaks appearing at $s/s_0 = 0.36$ and 0.68 , which respectively correspond to maximum thickness values of $t = 0.61\text{mm}$ and $t = 0.88\text{mm}$.

3.1.2. Experimental apparatus

To reduce the volume enclosed by the thin shell and monitor the pressure evolution acting on it, we assembled the experimental setup shown in Fig. 4. Its main components include a polypropylene syringe to extract the air inside the shell at a controlled flow rate, a Bose ElectroForce 3510 tester (Bose Corporation, Framingham, Massachusetts) used to impart a displacement load on the piston of the syringe, an acrylic fixture to constrain any sample movement, along with a pressure sensor (SM9333, SMI, California) and a microcontroller (Arduino UNO, Arduino, Italy). The thin elastic shell was mounted on an acrylic fixture, which consists of two supporting plates. The upper round plate had a circular hole at the center, with radius slightly larger than the radius of the hemispherical shell R . The thick band at the bottom of the shell was clamped between the acrylic plates, whereas the hemispherical part of the thin shell was allowed to freely deform without entering

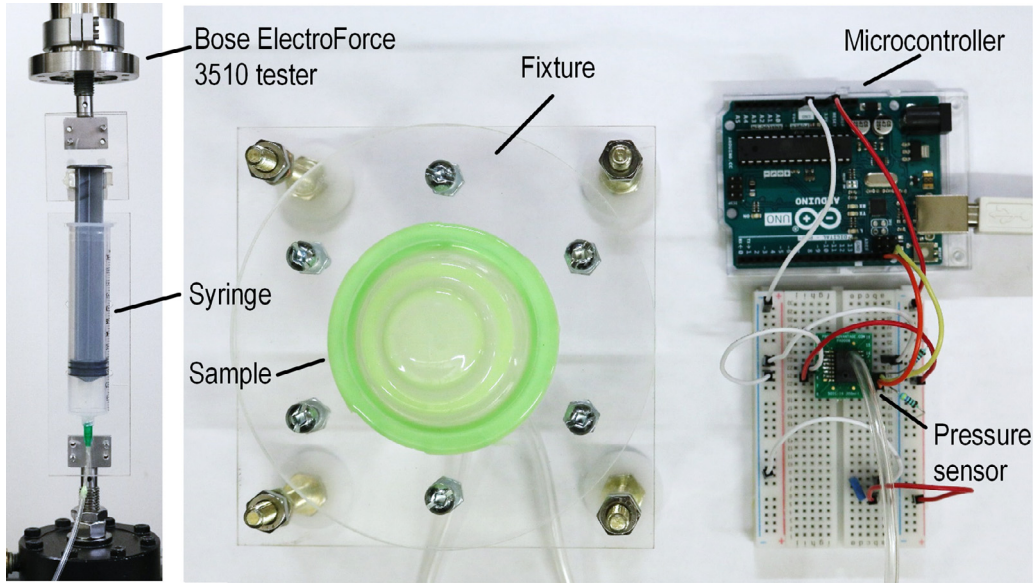


Fig. 4. Experimental setup: the shell sample is mounted on the basal fixture and connected with two hollow rubber tubes, one to the syringe and the other to the pressure sensor. The syringe is pulled by the Bose ElectroForce 3510 tester to extract air at a constant flow rate of 54 ml/s. A microcontroller regulates the operation of the pressure sensor which measures the internal pressure of the shell.

Table 3
Convergence of flow rate.

Flow rate (ml/s)	13	27	54	108	215
Snap through pressure (Pa)	13.55	13.64	13.88	13.82	14.03
Maximum pressure (Pa)	32.05	32.32	32.68	33.38	33.15

in contact with the fixture. The upper plate was tightly fastened to the lower acrylic plate with six equally spaced screws to prevent any leakage of air. The lower square plate was connected to the syringe and the pressure sensor. The syringe extracted air from the shell at a constant flow rate of 54 ml/s and was pulled by the Bose ElectroForce 3510 tester with displacement control at a constant speed. The sensor had a calibrated pressure range from -125 Pa to 125 Pa and a typical accuracy of $\pm 0.5\%$ of the full pressure span, which is ± 1.25 Pa. The pressure sensor was controlled by the microcontroller, which was programmed to read the pressure data from the sensor at a frequency of 20Hz.

The testing results from our experiments converged at a flow rate of 54 ml/s (Table 3). When the flow rate was decreased further, the variations in the snap-through pressure and the maximum pressure were below 0.33 Pa and 0.63 Pa, values below the accuracy of the sensor (± 1.25 Pa).

3.2. Theoretical model

A number of formulations exist in the literature for predicting the buckling pressure of elastic thin shells. Among them for shells undergoing small strains of the middle surface and moderate rotations, approximate expressions of the stretching and bending strains, e.g. the small strain-moderate rotation theory (Hutchinson, 2016) and the Donnell–Mushtari–Vlasov (DMV) theory (Budiansky, 1968; Hutchinson, 2016; Koiter, 1966, 1967; Sanders, 1963), can be used to predict buckling pressure. These theories are accurate for perfect spherical shells, but their precision degrades for shells with relatively large displacements and rotations (Hutchinson, 2016). Because the shells examined in this work experience large displacements and rotations, we use exact expressions of the Lagrangian stretching strains and changes in curvature as well as live pressure, i.e. the force per current area acting normal to the deformed middle surface, and compute the potential energy of the pressure. We assume the constitutive relation to be linear due to the small strains involved, and present a formulation that enables us to write the shell buckling equations without any restrictions on the magnitude of displacements and rotations (Hutchinson, 2016; Niordson, 1985). Furthermore, we follow the tensor analysis given by Niordson (1985) as well as Koiter and van der Heijden (2009) (see Appendix B) to derive the nonlinear buckling equations of the middle surface for axisymmetric deformations. The following section presents first the theory for spherical shells with perfect geometry, while Section 3.2.2 provides the formulation for shells with large imperfection. Appendix C reports the numerical method used to obtain the solutions.

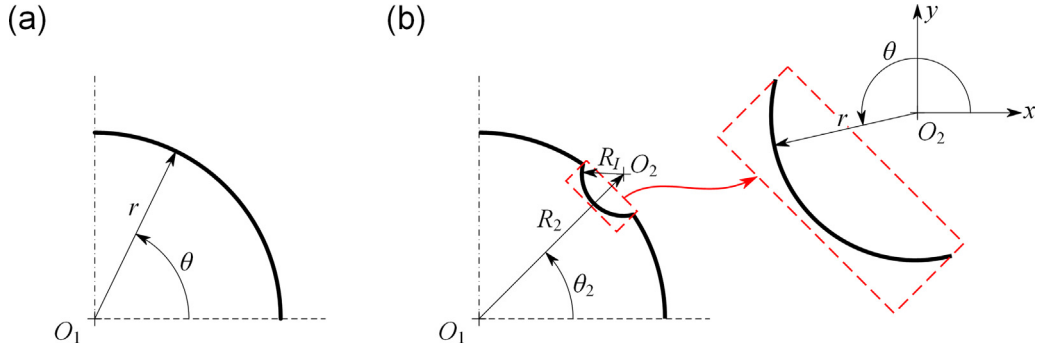


Fig. 5. Definition of coordinates θ and r : (a) Euler coordinate system (θ, ω, r) for a spherical shell; (b) modified Euler coordinate system (θ, ω, r) for shell with large imperfection. The thick line refers to the shell middle surface.

3.2.1. Shell theory for axisymmetric deformations of a spherical shell

Fig. 5a shows the Euler coordinates (θ, ω, r) for a perfect spherical shell. θ is the meridional angle, ω is the circumferential angle (not shown), and r is the distance from the origin O_1 . The meridional angle θ is measured from the equator ($\theta = 0$) to the upper pole ($\theta = \pi/2$). R is the radius of the shell and (θ, ω, R) represents the coordinates of a material point on the middle surface of the shell. For the deformed shell, the location of a material point on the middle surface is

$$\bar{\mathbf{r}} = u_\theta \mathbf{i}_\theta + u_\omega \mathbf{i}_\omega + (R + w) \mathbf{i}_r \quad (2)$$

where (u_θ, u_ω, w) are the displacements tangent and normal to the undeformed middle surface, and $(\mathbf{i}_\theta, \mathbf{i}_\omega, \mathbf{i}_r)$ are the corresponding unit vectors. For axisymmetric deformations, the circumferential displacement is null ($u_\omega = 0$), and the other two displacements, u_θ and w , are independent of the circumferential angle ω .

The nonlinear middle surface strains and the change in curvature of the middle surface are functions of the linear components of both strains $(e_{\theta\theta}, e_{\omega\omega}, e_{\theta\omega})$ and rotations $(\varphi_\theta, \varphi_\omega, \varphi_r)$, the former given by

$$\begin{aligned} e_{\theta\theta} &= \frac{1}{R} \left(\frac{\partial u_\theta}{\partial \theta} + w \right) \\ e_{\omega\omega} &= \frac{1}{R} \left(\frac{1}{\cos \theta} \frac{\partial u_\omega}{\partial \omega} - \tan \theta u_\theta + w \right) \\ e_{\theta\omega} &= \frac{1}{2R} \left(\frac{\partial u_\omega}{\partial \theta} + \frac{1}{\cos \theta} \frac{\partial u_\theta}{\partial \omega} + \tan \theta u_\omega \right) \end{aligned} \quad (3)$$

where the circumferential displacement u_ω and the partial derivatives with respect to the circumferential angle ω in $e_{\omega\omega}$ and $e_{\theta\omega}$ equal to zero for axisymmetric deformations. On the other hand, the latter, i.e. the linear rotations about the tangents and the normal to the middle surface are:

$$\begin{aligned} \varphi_\theta &= \frac{1}{R} \left(\frac{\partial w}{\partial \theta} - u_\theta \right) \\ \varphi_\omega &= \frac{1}{R} \left(\frac{1}{\cos \theta} \frac{\partial w}{\partial \omega} - u_\omega \right) \\ \varphi_r &= \frac{1}{2R} \left(\frac{\partial u_\omega}{\partial \theta} - \frac{1}{\cos \theta} \frac{\partial u_\theta}{\partial \omega} - \tan \theta u_\omega \right) \end{aligned} \quad (4)$$

For axisymmetric deformations, the non-vanishing components of the nonlinear middle surface strains and bending strains are given by

$$\begin{aligned} E_{\theta\theta} &= e_{\theta\theta} + \frac{1}{2} e_{\theta\theta}^2 + \frac{1}{2} \varphi_\theta^2 \\ E_{\omega\omega} &= e_{\omega\omega} + \frac{1}{2} e_{\omega\omega}^2 \end{aligned} \quad (5)$$

and

$$\begin{aligned} K_{\theta\theta} &= \frac{1}{R} \left[(1 + e_{\theta\theta} + e_{\omega\omega} + e_{\omega\omega} e_{\theta\theta}) \left(-1 + \frac{\partial \varphi_\theta}{\partial \theta} - e_{\theta\theta} \right) - \varphi_\theta (1 + e_{\omega\omega}) \left(\frac{\partial e_{\theta\theta}}{\partial \theta} + \varphi_\theta \right) + 1 \right] \\ K_{\omega\omega} &= \frac{1}{R} [(1 + e_{\theta\theta} + e_{\omega\omega} + e_{\omega\omega} e_{\theta\theta}) (-1 - \tan \theta \varphi_\theta - e_{\omega\omega}) + \tan \theta \varphi_\theta (1 + e_{\omega\omega}) (e_{\theta\theta} - e_{\omega\omega}) + 1] \end{aligned} \quad (6)$$

We note that in Eqs. (4) and (6), the sign of both rotation and change in curvature is opposite to that of previous works (Budiansky, 1968; Hutchinson, 2016; Lee et al., 2016b; Sanders, 1963), because here the definition of rotation and curvature

change follow that of [Niordson \(1985\)](#). For axisymmetric deformations, the last two terms in [Eq. \(4\)](#) vanish, i.e. $\varphi_\omega = 0$ and $\varphi_r = 0$.

The resultant membrane stresses $(N_{\theta\theta}, N_{\omega\omega}, N_{\theta\omega})$ and the bending moments $(M_{\theta\theta}, M_{\omega\omega}, M_{\theta\omega})$ for a shell with isotropic linear elastic material are

$$\begin{aligned} N_{\alpha\beta} &= \frac{Et}{(1-\nu^2)} [(1-\nu)E_{\alpha\beta} + \nu E_{\gamma\gamma} \delta_{\alpha\beta}] \\ M_{\alpha\beta} &= D[(1-\nu)K_{\alpha\beta} + \nu K_{\gamma\gamma} \delta_{\alpha\beta}] \end{aligned} \quad (7)$$

where E is the Young's modulus, t is the shell thickness, ν is the Poisson's ratio, and $D = Et^3/[12(1-\nu^2)]$ is the bending stiffness. The subscripts in [Eq. \(7\)](#) take on values 1 or 2, and the Einstein summation convention applies. The non-vanishing components in the membrane stress and bending moments are $(N_{\theta\theta}, N_{\omega\omega})$ and $(M_{\theta\theta}, M_{\omega\omega})$.

The sum of the stretching and bending energy gives the elastic strain energy (SE) expressed as:

$$SE(u_\theta, w) = \frac{1}{2} \int_S (M_{\alpha\beta} K_{\alpha\beta} + N_{\alpha\beta} E_{\alpha\beta}) dS \quad (8)$$

where S is the area of the perfect spherical surface in its undeformed state ([Fig. 5a](#)).

The potential energy of the uniform external pressure is

$$PE = p\Delta V \quad (9)$$

where ΔV is the volume change. For small deformations, the volume change can be approximated with the pressure acting on the initial middle surface in the direction normal to the initial middle surface, namely the dead pressure:

$$\Delta V(u_\theta, w) = \int_S w dS \quad (10)$$

For large axisymmetric deformations, the volume change ΔV is obtained with the pressure acting on the deformed middle surface in the direction normal to the deformed middle surface, i.e. the live pressure, whose exact expression is here derived as:

$$\Delta V(u_\theta, w) = \int_S \left\{ w + \frac{1}{2} [w(e_{\theta\theta} + e_{\omega\omega}) - \varphi_\theta u_\theta] + \frac{1}{3} (w e_{\theta\theta} e_{\omega\omega} - e_{\omega\omega} \varphi_\theta u_\theta) \right\} dS \quad (11)$$

[Eq. \(11\)](#) contains both the linear term, i.e. dead pressure, and the products of displacements, rotations and strains. While the former term only is sufficient to study the buckling pressure of perfect spherical shells ([Hutchinson, 2016](#); [Lee et al., 2016b](#)), the latter cannot be neglected for a shell with pole displacement comparable to its radius, which experiences large nonlinear deformation, as is the case of the shell examined here.

The total potential energy Ψ of the spherical shell is given by the sum of the elastic strain energy SE and the potential energy PE of the external pressure

$$\Psi(u_\theta, w) = SE + PE \quad (12)$$

3.2.2. Imperfect shell theory for axisymmetric deformations

To account for the large geometric imperfection (axisymmetric circular-arc), we introduce the modified Euler coordinates (θ, ω, r) shown in [Fig. 5b](#). Here, the difference from the Euler coordinate system ([Fig. 5a](#)) pertains to the coordinates θ and r , which are defined with respect to the center of the imperfection O_2 , rather than the origin of the Euler coordinate system O_1 . Following the geometry parameters introduced in [Section 2](#), the coordinates of O_2 (θ_2, ω, R_2) are given by

$$\begin{aligned} \theta_2 &= \theta_m \\ R_2 &= R \cos \frac{\theta_w}{2} - 2R \sin \frac{\theta_w}{2} \frac{h}{l} + R \sin \frac{\theta_w}{2} \left(\frac{l}{4h} + \frac{h}{l} \right) \end{aligned} \quad (13)$$

In the general case, the coordinates of a material point on the middle surface of the imperfection is (θ, ω, R_l) , where the radius of the imperfection, R_l ([Fig. 5b](#)), is given by:

$$R_l = R \sin \frac{\theta_w}{2} \left(\frac{l}{4h} + \frac{h}{l} \right) \quad (14)$$

The location of a material point on the deformed middle surface of the imperfection is

$$\bar{\mathbf{r}} = R_2 \mathbf{i}_2 + u_\theta \mathbf{i}_\theta + u_\omega \mathbf{i}_\omega + (R_l + w) \mathbf{i}_r \quad (15)$$

where $R_2 \mathbf{i}_2$ is the location of the center of the imperfection, (u_θ, u_ω, w) are the displacements tangent and normal to the undeformed middle surface, and $(\mathbf{i}_\theta, \mathbf{i}_\omega, \mathbf{i}_r)$ are the corresponding unit vectors. For axisymmetric deformations, the circumferential displacement equals to zero $u_\omega = 0$, and the other displacements, u_θ and w , are independent of the circumferential angle ω .

The nonlinear strains and the change in curvature of the middle surface are functions of the linear components of the strains ($e_{\theta\theta}$, $e_{\omega\omega}$, $e_{\theta\omega}$) and the rotations (φ_θ , φ_ω , φ_r), the former given by:

$$\begin{aligned} e_{\theta\theta} &= \frac{1}{R_l} \left(\frac{\partial u_\theta}{\partial \theta} + w \right) \\ e_{\omega\omega} &= \frac{1}{R_l \cos \theta + R_2 \cos \theta_2} \left(\frac{\partial u_\omega}{\partial \omega} - \tan \theta u_\theta + \cos \theta w \right) \\ e_{\theta\omega} &= \frac{1}{2R_l(R_l \cos \theta + R_2 \cos \theta_2)} \left[(R_l \cos \theta + R_2 \cos \theta_2) \frac{\partial u_\omega}{\partial \theta} + R_l \frac{\partial u_\theta}{\partial \omega} + R_l \sin \theta u_\omega \right] \end{aligned} \quad (16)$$

For axisymmetric deformations, the circumferential displacement u_ω and the partial derivatives with respect to the circumferential angle ω in $e_{\omega\omega}$ and $e_{\theta\omega}$ equal to zero.

The linear rotations about the tangents and normal of the middle surface are expressed as:

$$\begin{aligned} \varphi_\theta &= \frac{1}{R_l} \left(\frac{\partial w}{\partial \theta} - u_\theta \right) \\ \varphi_\omega &= \frac{1}{R_l \cos \theta + R_2 \cos \theta_2} \left(\frac{\partial w}{\partial \omega} - \cos \theta u_\omega \right) \\ \varphi_r &= \frac{1}{2R_l(R_l \cos \theta + R_2 \cos \theta_2)} \left[(R_l \cos \theta + R_2 \cos \theta_2) \frac{\partial u_\omega}{\partial \theta} - R_l \frac{\partial u_\theta}{\partial \omega} - R_l \sin \theta u_\omega \right] \end{aligned} \quad (17)$$

For axisymmetric deformations, the last two terms vanish ($\varphi_\omega = 0$ and $\varphi_r = 0$), whereas the non-vanishing components of the nonlinear middle surface strains for axisymmetric deformations are given by Eq. (5). The non-vanishing changes in curvature for axisymmetric deformations are

$$\begin{aligned} K_{\theta\theta} &= \frac{1}{R_l} \left[(1 + e_{\theta\theta} + e_{\omega\omega} + e_{\omega\omega} e_{\theta\theta}) \left(-1 + \frac{\partial \varphi_\theta}{\partial \theta} - e_{\theta\theta} \right) - \varphi_\theta (1 + e_{\omega\omega}) \left(\frac{\partial e_{\theta\theta}}{\partial \theta} + \varphi_\theta \right) + 1 \right] \\ K_{\omega\omega} &= \frac{\cos \theta}{R_l \cos \theta + R_2 \cos \theta_2} \left[(1 + e_{\varphi\varphi} + e_{\omega\omega} + e_{\omega\omega} e_{\varphi\varphi}) \left(-1 - \tan \theta \varphi_\theta - e_{\omega\omega} \right) \right. \\ &\quad \left. + \tan \theta \varphi_\theta (1 + e_{\omega\omega}) (e_{\theta\theta} - e_{\omega\omega}) + 1 \right] \end{aligned} \quad (18)$$

From a comparison of Eqs. (16)–(18) with Eqs. (3), (4) and (6), we find that the linearized strains of the middle surface, the linearized rotation and the change in curvature of the imperfection, have expressions identical to those of a spherical shell with $R_l = R$ and $R_2 = 0$. This describes the limiting case, where the geometry of the imperfection becomes a sphere ($R_2 = 0$), and its size matches that of the spherical shell ($R_l = R$).

The stress strain relations, the elastic strain energy, the volume change for live pressure, and the total potential energy are then given by Eqs. (7), (8), (11), and (12).

3.3. Finite element modelling

To investigate the shell response controlled by an imperfection varying in size and location, a set of FEM simulations (ABAQUS/STANDARD) were also conducted in parallel to the experimental and theoretical work described above. The complementary results not only provide context for validation but also serve to study shell sensitivity to defect amplitude and position as well as radius to thickness ratio (Section 4.2). For the base material (VPS elastomer), we adopted an incompressible neo-Hookean model, whose coefficients were calculated from previously obtained measures (Pezzulla et al. (2015) of Young's modulus and Poisson's ratio (Table 2). Clamped boundary conditions were applied at the equator of the hemispherical shell, while a uniform external pressure was imposed on the outer surface of the shell. Due to the unstable post-buckling behavior, the search for the equilibrium path was carried out through the modified Riks method (Riks, 1979).

Two geometries were examined for the shell. The first replicates the non-uniform thickness (Fig. 3b) induced by the manufacturing process (see Appendix A for inclusion of thickness variation), while the latter reproduces the ideal uniform thickness of the perfect shell, providing a baseline for comparison. Furthermore, since spherical shell deformation can be either axisymmetric or non-axisymmetric (Hutchinson, 2016), both scenarios were examined. For the former, the linear line element SAX1 was used due to its ability to capture only axisymmetric deformation, and for the latter, we built a three-dimensional model with two types of shell elements (linear quadrilateral shell elements S4R with reduced integration, and 3-node triangular shell elements S3R) that together can capture the non-axisymmetric deformation. A set of mesh convergence studies (Appendix D) was performed to determine the sufficient number of elements for each type: 80 elements for the SAX1 axisymmetric line element, and around 10000 for S4R and S3R shell elements.

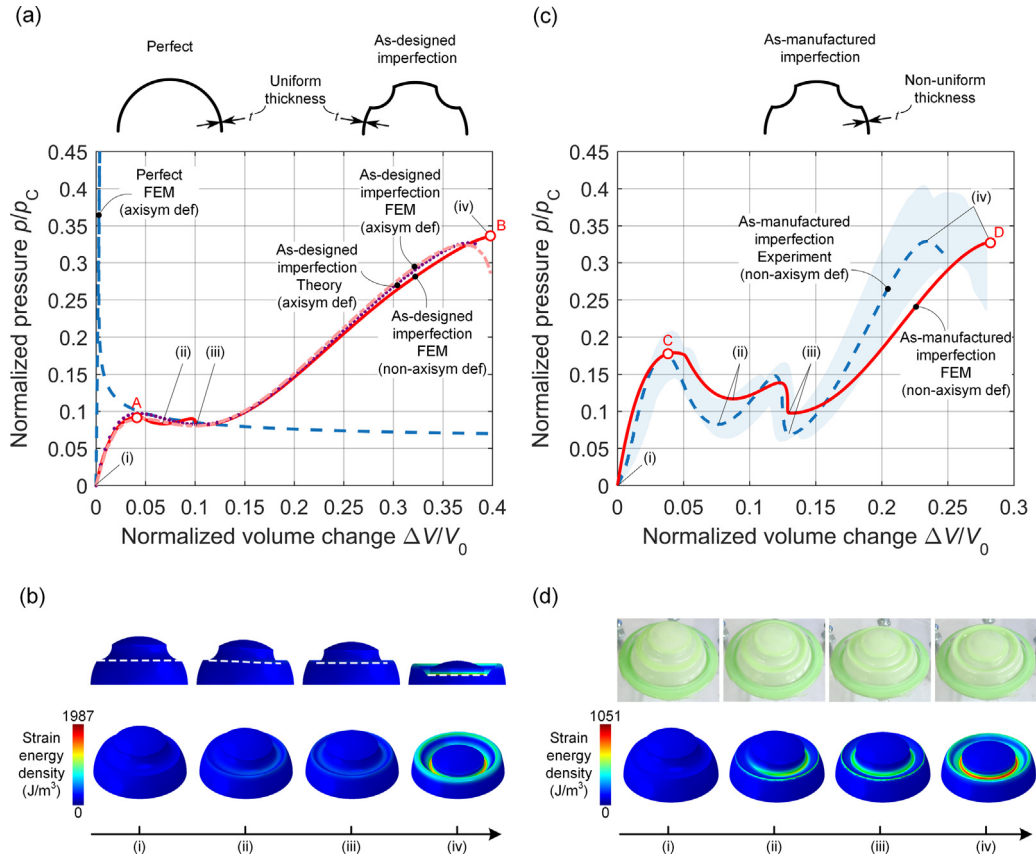


Fig. 6. Responses of perfect and imperfect spherical shells under uniform pressure. (a) Pressure versus change in volume for perfect and as-designed imperfect shell with uniform thickness, with volume change normalized by the negative of the volume within the middle surface of the undeformed hemisphere, $V_0 = -2\pi R^3/3$. Loss of stability for the perfect shell appears with a small volume change, as opposed to the imperfect shell, which remains stable post snap-through buckling for a wide range of volume change. The theoretical solution accounts for axisymmetric deformations, whereas non-axisymmetric modes are captured by FEM. (b) Cross-section view (above) and three-dimensional view (below) of deformed modes and corresponding strain energy density of as-designed imperfect shell with uniform thickness. Changes in the inclination of the horizontal dashed lines below the cap indicate buckling transition from axisymmetric to a non-axisymmetric mode. (c) Pressure versus change in volume obtained from experiment and FEM simulation for as-manufactured imperfect shell with as-measured non-uniform thickness. (d) Deformed configurations from experiments on shell samples (above) and FEM accounting for non-axisymmetric deformations in as-built shell samples (below) along with corresponding strain energy density.

4. Results and discussion

4.1. Buckling of imperfect spherical shells with large axisymmetric imperfection

We present here a set of theoretical, computational and experimental results of the shell response to a uniform externally applied pressure under two scenarios: i) as-designed imperfection with a priori assumed thickness (uniform profile), and ii) as-built imperfection with actual thickness variation induced by manufacturing (non-uniform profile).

4.1.1. Effects of as-designed and as-manufactured imperfections

Fig. 6a shows the baseline response of a perfect hemispherical shell along with that of a shell with as-designed imperfection with uniform thickness and shell geometry given in Table 1. The blue dashed line is for the perfect baseline hemispherical shell and represents the classical buckling response extensively investigated in literature (Hutchinson, 2016; Wagner et al., 2018). Normalized with the Zoelly's buckling pressure $p_c = 2E(t/R)^2/\sqrt{3(1-\nu^2)}$ (Zoelly, 1915), the pressure rapidly increases with tiny changes in volume up to unity. Post bifurcation, a monotonic plunge of pressure appears, followed by a gradually descending plateau (just below 0.1) that spans the entire range of $\Delta V/V_0$.

The purple and red curves in Fig. 6a refer to the imperfect shell with as-designed uniform thickness. The former (purple dots) is the pressure provided by our theoretical model (Section 3.2), which assumes axisymmetric deformations, and the latter (red) that obtained by our numerical models (Section 3.3), one accounting for axisymmetric (dash-dot) and the other for non-axisymmetric (solid line) deformation. For axisymmetric deformations, the difference between theoretical and FEM models is below 1%. In addition, the responses from the FEM models for both axisymmetric and non-axisymmetric deformations are well aligned with 3.6% relative difference in maximum pressure, a result implying shell deformation being close

to axisymmetric. At the volume change of $\Delta V/V_0 = 0.04$, the pressure of the imperfect shell enters a region of snap-through buckling, after which the pressure monotonically increases to reach a maximum value of $p/p_c = 0.34$ at $\Delta V/V_0 = 0.40$.

The divergence between axisymmetric and non-axisymmetric modes occurs at the snap-through region, where the FEM simulation captures an additional peak, which can be attributed to the non-axisymmetric buckling mode. This is shown in Fig. 6b; here the sequential stages of deformation reveal the start of a buckling transition mode from axisymmetric to non-axisymmetric, the latter requiring lower strain energy than the former and hence most likely to appear. The second peak corresponds to the return of the deformation to the axisymmetric response. After the second peak, the value of pressure gradually approaches the solution of our theoretical model for axisymmetric deformations. Despite the qualitative difference between the red and purple curves, the pressure value of the second peak is only 10% higher than the pressure value at the identical volume change predicted by the theoretical and FEM models for axisymmetric deformations. This result suggests that the axisymmetric mode can provide a sufficient level of approximation for shell design.

A number of differences emerge between the perfect and imperfect shell shown in Fig. 6a. The main one is their buckling mode. The imperfect shell first undergoes snap-through buckling at a pressure lower than the maximum pressure, and then it regains stability as the pressure increases to the maximum, a phenomenon not observed in the perfect spherical counterpart. The perfect shell undergoes bifurcation buckling for a tiny value (below 1%) of the normalized volume change, where the pressure reaches its maximum without undergoing snap-through instability. After the bifurcation point, the post-buckling pressure decreases monotonically until the shell is everted, thereby denying the chance for the shell to regain stability (Gomez et al., 2019; Hutchinson, 2016; Taffetani et al., 2018).

Maximum pressure and corresponding volume change are other attributes (besides the buckling mode) that differ in value between the perfect and imperfect shells (Fig. 6a). The maximum pressure in the imperfect case (point B) decreases to 34% of the theoretical maximum pressure ($p/p_c = 1$) of the perfect shell baseline (not shown in figure). This drop is minor compared to the buckling pressure of perfect shells fabricated with conventional processes; for perfect shells, the experimental values measured in the literature show a large spread with severe drops (up to 90%) from the ideal case (Lee et al., 2016b; Wagner et al., 2018). These well-known results attest to the large sensitivity of perfect shells to geometric defects. On the other hand, the imperfect shell under investigation in this study can provide a maximum pressure value (point B) comparable to that of its perfect counterpart. A similar observation applies to its impact on the volume change. For the perfect hemispherical shell, a tiny value of $\Delta V/V_0 < 0.01$ is required to attain maximum pressure before proceeding spontaneously to catastrophic collapse without an increase in the magnitude of the applied pressure. In contrast, the imperfect shell after the first peak features a gradual and stable response over a large volume change, thereby demonstrating its capacity to resist deformation upon an increase of the applied pressure up to the maximum pressure value reached at $\Delta V/V_0 = 0.40$.

Fig. 6b shows sequential stages of deformation for the imperfect shell with uniform thickness (solid red curve in Fig. 6a). At the onset, the shell stays axisymmetric, and its cap reseats without tilting, as shown by the white dashed line tracing the bottom of the imperfection. When the pressure reaches the first peak, a non-axisymmetric response starts to develop. As illustrated in Fig. 6b (ii), with an increase of the volume change the strain energy density localizes on the right-hand side of the imperfection, and the cap sinks with a tilt to the right hand side. Here the strain energy refers to the energy stored in the shell due to stretching and bending. After the second buckling peak, the localized strain energy starts to propagate circumferentially along the axisymmetric imperfection. At the second local minimum of pressure, the left-hand side of the imperfection also tilts until its height equals that of the right-hand side (Fig. 6c (iii)). From this stage onward, shell axisymmetry is preserved and no further changes in deformation mode occur up to the maximum pressure (Fig. 6c (iv)).

Thickness non-uniformity (Fig. 2) caused by the fabrication process is another factor influencing the snap-through buckling, as shown in Fig. 6c. The dashed blue line represents the experimental measure of the normalized pressure for one representative sample, and the shaded domain (light blue) is the envelope of responses generated by the eight samples here tested. Similar to Fig. 6a, the imperfect shell first undergoes snap-through buckling with two local peaks in pressure, followed by a stable response that requires additional deformation to reach the maximum pressure. Aligned with the experimental curves is the computationally obtained response in red with two peaks in pressure in the snap-through region that capture non-axisymmetric deformation. By comparing the solid line curves for the imperfect shell in Figs. 6a and c, we can gain insights into the effect of thickness variation on the maximum pressure (point B versus point D) and its corresponding volume change, as well as the snap through pressure (point A versus point C). For the maximum pressure, the deviation is minor (2%) and it occurs with relatively modest change of volume change (29%). This infers a minor sensitivity of the maximum pressure to thickness variations. For the snap through pressure, on the other hand, the impact is severe (93% increase) attesting a high sensitivity as opposed to the volume change which is almost unaffected (5% difference).

Similar to the as-designed imperfect shell (Fig. 6b), Fig. 6d shows snapshots of deformation for the as-manufactured shells obtained from experiments (above) and FEM (below). After the first snap-through (Fig. 6d (ii)), the as-manufactured shell undergoes non-axisymmetric buckling, characterized by strain energy localization mainly in the middle of a given cross-section of the large imperfection. After the second snap-through, the deformation returns to an axisymmetric mode (Fig. 6d (iii)) until the pressure reaches the maximum (Fig. 6d (iv)).

In general, the results presented above from shell theory, experiments and FEA are very well aligned with a maximum 5.9% relative difference in maximum pressure. We attribute the reason for these deviations to other imperfections that might be present in our samples but that were neglected in our models. During fabrication, defects intrinsic to the manufacturing process, such as thickness variation along the meridional and circumferential direction, geometric imperfections of the

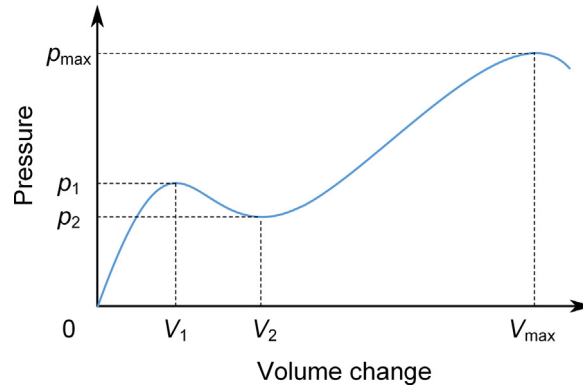


Fig. 7. Pressure-volume change response of an imperfect shell undergoing axisymmetric deformations. The pressures at the limit points p_1 and p_2 along with the volume change V_1 and V_2 are introduced to describe the snap-through behavior.

mold, and impurities in the base material, e.g. microvoids, might appear and contribute to the mild departure from the experimental results (Lee et al., 2016b). In addition, the thickness profile, which was modelled with a relative high level of accuracy (see Appendix A), is still an approximation that could play a role in overestimating the minimum pressure in the snap-through region (Fig. 6c).

4.2. Sensitivity to as-designed large geometric imperfection

Here we investigate the buckling sensitivity of a uniform thickness shell with an as-designed imperfection to a set of defects varying in size and location within its hemispherical geometry. We focus on axisymmetric deformations only, given that Section 4.1 has shown the assumption of axisymmetric deformation leads to a deviation of the normalized maximum pressure of 3.6% from the non-axisymmetric case, hence retaining a sufficient level of accuracy for the study here undertaken.

Let us first define the parameters governing the snap-through buckling response for an imperfect shell with axisymmetric deformation. Fig. 7 shows a representative response of pressure-volume change, where p_1 and p_2 specify the pressure at the limit points of the initial snap-through buckling, and p_{\max} represents the obtainable maximum pressure. For the metrics here used, we adopt the normalized maximum pressure p_{\max}/p_C , the snap-ratio $|p_1 - p_2|/p_1$, and the ratio between snap-through pressure and the maximum pressure p_1/p_{\max} , along with their counterparts in volume change V_{\max}/V_0 , $|V_1 - V_2|/V_1$, and V_1/V_{\max} . p_C is Zoelly's buckling pressure. V_0 is the volume of a perfect hemisphere. The definition of these snap ratios enables the assessment of the relative difference in pressure and volume change between the limit points of the snap-through buckling branch (Vieira et al., 2017).

Although the large imperfection here presented applies also to degenerate imperfect shells reducing to a cone (Fig. 1f), in this section we restrict our sensitivity study to hemispherical geometries with imperfection parameters falling within given geometric ranges. Specifically, the angular width θ_w is assumed to range from 2.4° to 24° , the amplitude h/l from 0.05 to 0.5, the meridional angle θ_m from 30° to 70° , and the radius to thickness ratio R/t from 20 to 150. We prescribe also the radius of the shell to be $R = 25$ mm. To ease a systematic interpretation of the results, we divide the other four geometric parameters into two groups. The first describes the size of the imperfection, including the angular width θ_w and the amplitude h/l . The second designates the location of the imperfection and the slenderness of the shell, including the meridional angle θ_m and the radius to thickness ratio R/t . The study then is carried out by exploring the impact of changing the values of one group at a time, i.e. assuming the parameters of the other group are given.

4.2.1. Sensitivity to imperfection size

Here, the imperfection size is meant to describe changes in both the angular width θ_w ranging from $\theta_w = 2.4^\circ$ to 24° and the defect amplitude h/l spanning the interval from 0.05 to 0.5. These are the variables, as opposed to the meridional angle and the radius to thickness ratio which are prescribed ($\theta_m = 45^\circ$ and $R/t = 100$).

Fig. 8 shows four possible modes for the imperfect shell to respond to pressure. We classify them with respect to the deformation mechanism that corresponds to the maximum pressure achievable within the entire response, i.e. the curve: p/p_C versus $\Delta V/V_0$. Mode 1 resembles the classical instability of a perfect spherical, i.e. an inward dimple-like shape (Fig. 8a) and it is governed by small values of the imperfection (e.g. $\theta_w = 4.6^\circ$ and $h/l = 0.1$) (Audoly and Hutchinson, 2019; Hutchinson, 2016). Here the pressure first increases linearly up to the bifurcation point $p/p_C = 0.81$ at $\Delta V/V_0 = 0.01$, before dropping abruptly to a plateau around $p/p_C = 0.1$. Post bifurcation, there is a deviation in pressure at $\Delta V/V_0 = 0.18$, which is caused by the dimple deformation reaching and interacting with the imperfection, a secondary phenomenon that follows shell collapse. This is a secondary peak of pressure much smaller than the maximum value characterizing mode 1, hence it is of negligible significance. It should also be noted that for a real shell, the maximum pressure may be significantly reduced by other types of defects, e.g. small dimple at the pole, which might be introduced by the manufacturing process.

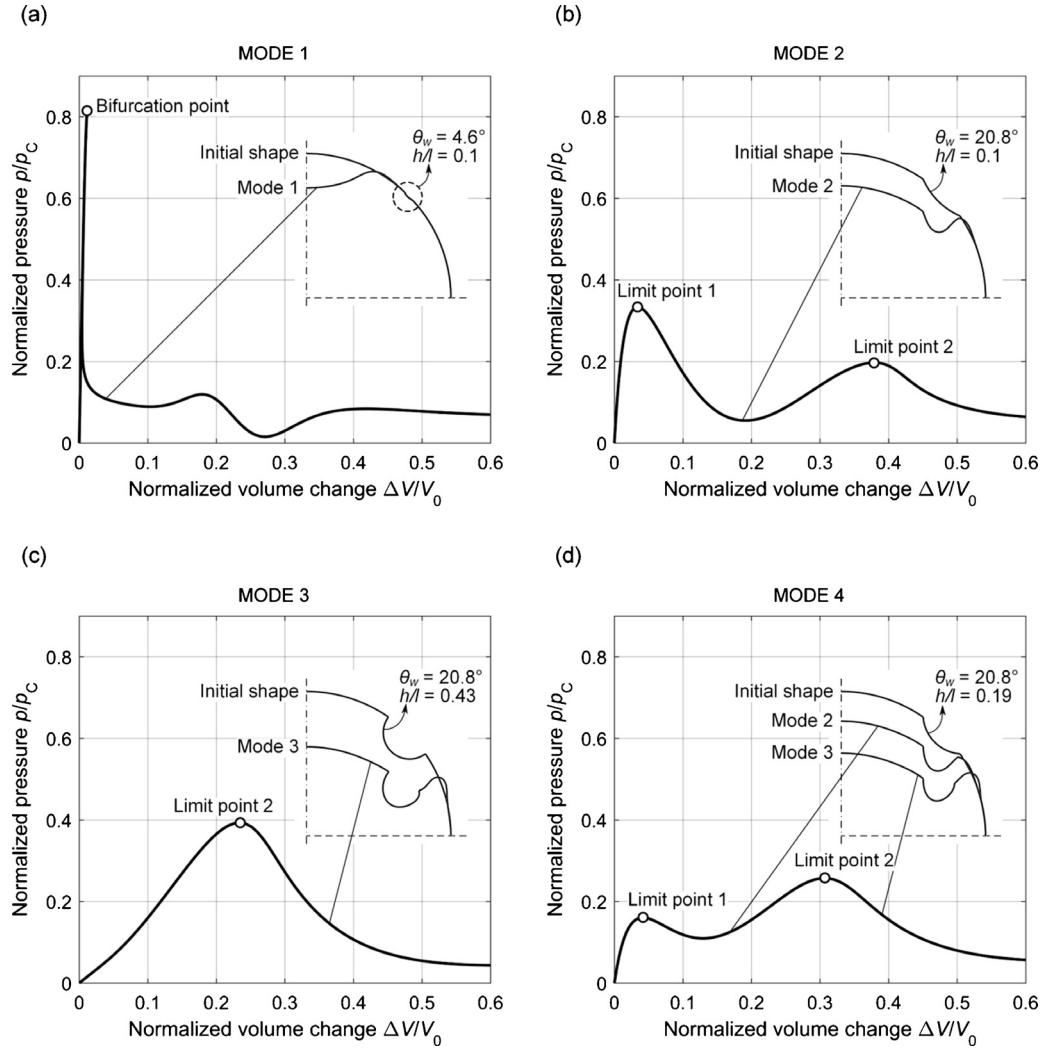


Fig. 8. Possible deformation modes leading to shell collapse. (a) Mode 1: Bifurcation buckling characterized by a dimple-like shape response. (b) Mode 2: Snap-through buckling 1 describing localized deformation within the imperfection. (c) Mode 3: Snap-through buckling 2 representative of localized deformation below the imperfection. (d) Mode 4: Snap-through buckling combining mode 2 and 3.

Mode 2 identifies a post-buckling response with deformation localized within the imperfection region (Fig. 8b). This mode indicates a transition from bifurcation to snap through buckling. It is governed by a larger imperfection size with values (e.g. $\theta_w = 20.8^\circ$ and $h/l = 0.1$) above a lower critical bound, as illustrated and further explained in a subsequent figure (Fig. 9). The pressure here increases monotonically to the maximum at the limit point 1 ($p/p_C = 0.33$) before starting to descend. While the pressure at the limit point 1 is much smaller than the bifurcation pressure in mode 1, the maximum volume change ($\Delta V/V_0 = 0.03$) is still close to that of mode 1. Following snap-through, the pressure may reach a second peak, i.e. limit point 2, at a larger volume change. Its value, however, does not define mode 2 because it is lower than the maximum attainable pressure, i.e. limit point 1, hence it is not considered further.

Fig. 8c illustrates mode 3, a snap-through buckling controlled by a localized deformation accrued below the imperfection. This response is caused by increasing values of the imperfection size (e.g. $\theta_w = 20.8^\circ$ and $h/l = 0.43$). Snap-through buckling occurs at limit point 2, which is the maximum attainable pressure ($p/p_C = 0.39$) achieved at $\Delta V/V_0 = 0.23$, a value much larger than that observed in mode 1 and 2.

For all of the aforementioned buckling modes (1, 2, and 3), the shell collapses once the prescribed pressure exceeds the buckling pressure. Mode 4 (Fig. 8d) is hybrid case combining modes 2 and 3. It describes a scenario where snap-through buckling with mode 2 arises before the attainment of the maximum pressure with mode 3. This behaviour is triggered by a large width and moderate amplitude of the imperfection (e.g. $\theta_w = 20.8^\circ$ and $h/l = 0.19$). In addition, this mode can also be triggered in full spheres that are not clamped at the equator (see Appendix E). Although the modes in Fig. 8 is obtained from one imperfection, they can also form a cascade of snap-through buckling in a shell with multiple imperfections (see Appendix F).

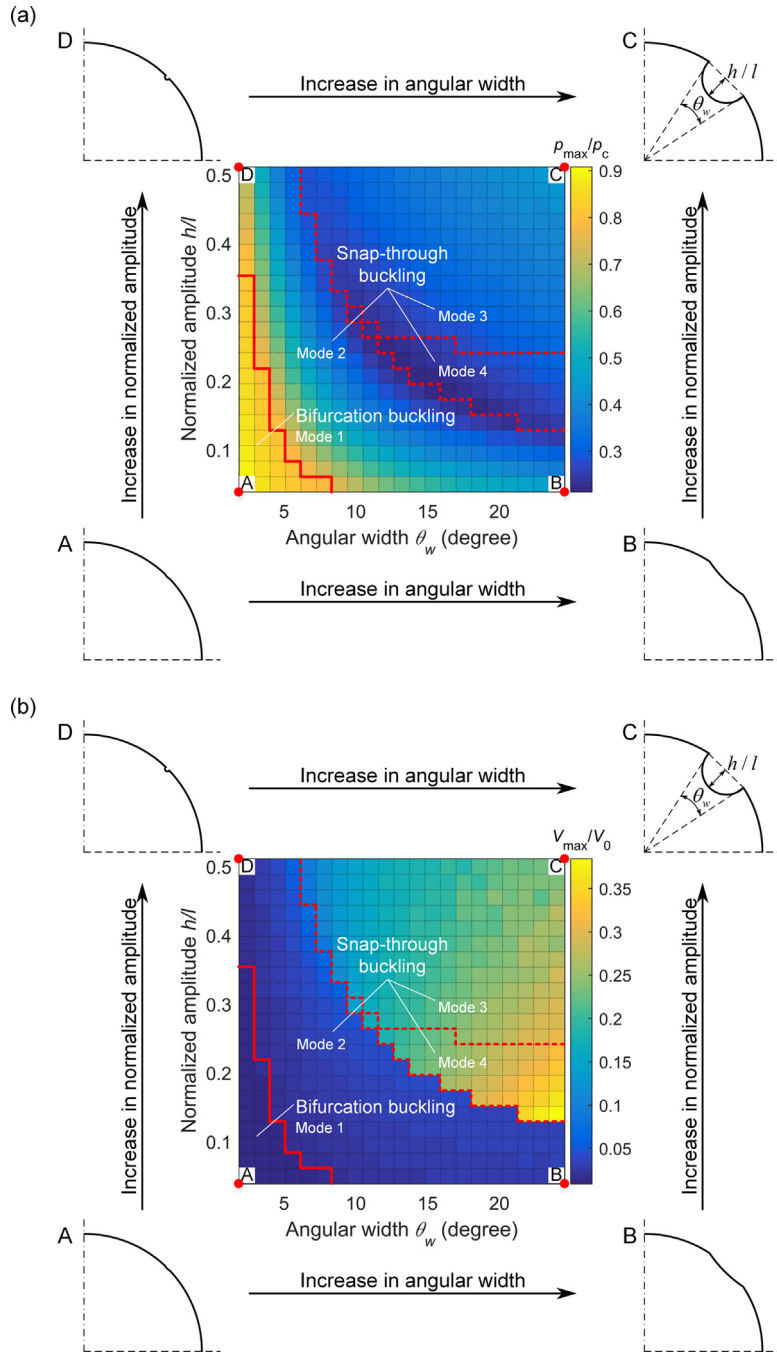


Fig. 9. Role of imperfection size on (a) the normalized maximum pressure and (b) the normalized volume change at the maximum pressure. With an increase in imperfection size, the buckling mode transitions from bifurcation buckling to snap-through buckling.

A map summarizing the buckling modes obtained for a range of combinations of imperfection width θ_w and amplitude h/l is shown in Fig. 9a. This map helps gain insight into the transition between buckling modes for a given set of imperfection parameters. From visual inspection, we gather that small imperfections lead to mode 1, visualized as the zone in the lower-left corner and below the solid red bound. Within this domain, the lower bounds of the two parameter ranges ($\theta_w = 2.4^\circ$ and $h/l = 0.05$), i.e. the smallest imperfection size, generate the highest maximum pressure ($p_{\max}/p_c = 0.91$), which approaches the theoretical buckling pressure of a perfect spherical shell. As the imperfection size increases, snap-through buckling becomes dominant and replaces bifurcation buckling. From the map, we further observe a set of buckling mode transitions, first to mode 2, and then to mode 4 and mode 3 as controlled by the geometric descriptors of the imperfection. For mode 2, the maximum pressure (at limit point 1) decreases monotonically – as it is the case for mode 1 – if

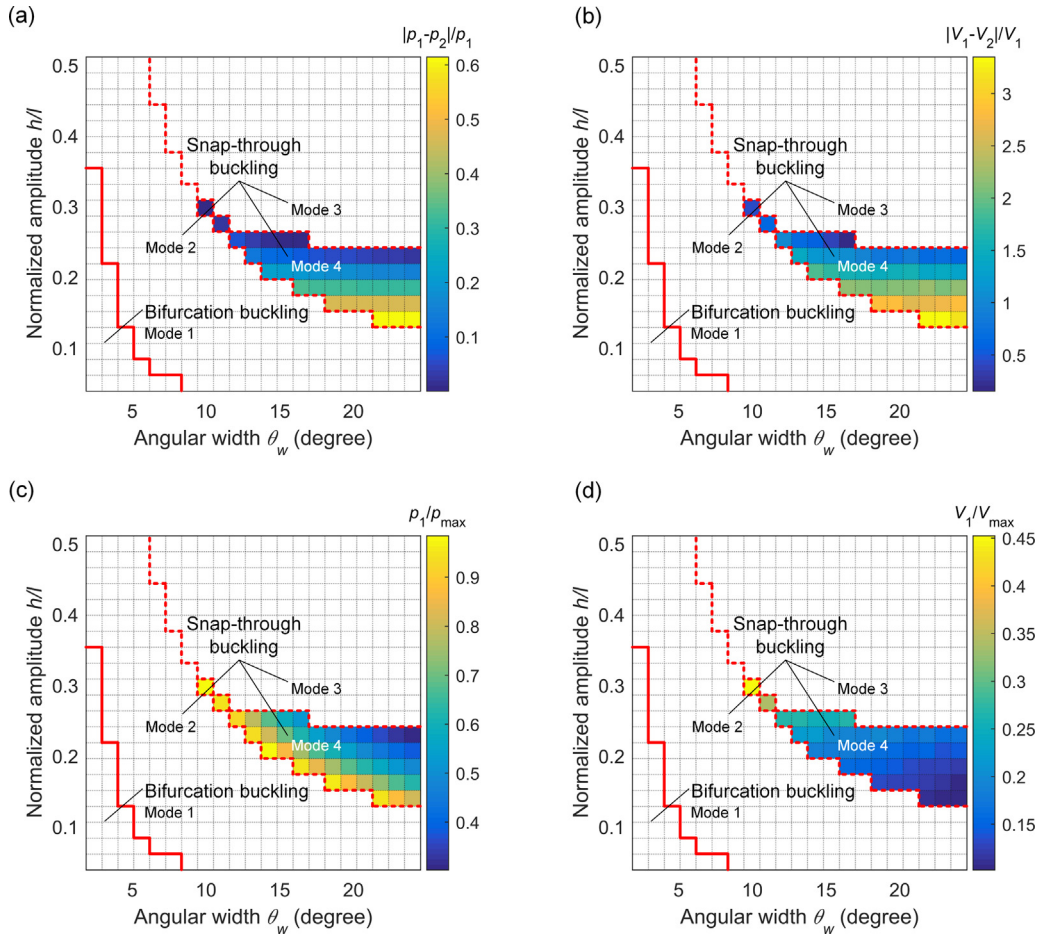


Fig. 10. Role of imperfection size on snap-through properties. (a) and (b) Snap ratios of pressure and volume change. (c) Ratio of snap-through pressure over maximum pressure. (d) Ratio of snap-through volume change against maximum volume change.

either the imperfection width θ_w or amplitude h/l is increased. When limit point 1 is lower than limit point 2, the buckling mode switches to mode 4, which combines modes 2 and 3. This mode is sandwiched between the zones of mode 3 and mode 2 on the middle-low part of the right hand side of the map, characterized by imperfections with large width θ_w and moderate amplitude h/l . As limit point 1 continues to decrease with increasing θ_w and h/l , it may disappear leaving limit point 2 as the only limit point. The buckling mode here switches to mode 3, which lies in the upper-right corner of the map. In both domains of mode 3 and mode 4, the maximum pressure is attained at limit point 2, and has a reversed trend with the maximum value increasing with both imperfection width and amplitude. The highest maximum pressure in these modes ($p_{\max}/p_C = 0.44$) appears at the upper-right corner for the largest imperfection size ($\theta_w = 24^\circ$ and $h/l = 0.5$).

Fig. 9b shows a corresponding map of the normalized maximum volume change. In mode 1 and 2, V_{\max}/V_0 is small, typically below 0.07, indicating that here the slightly imperfect shells start to collapse in a configuration resembling its undeformed state. For shells in mode 3 and mode 4, the maximum volume change is attained at limit point 2 with larger values ranging from $V_{\max}/V_0 = 0.08$ to $V_{\max}/V_0 = 0.38$. In these domains, the maximum volume change increases with the imperfection width θ_w and decreases with the amplitude h/l . In addition, V_{\max}/V_0 is continuous across the boundary between mode 2 and mode 3, but discontinuous across the boundary between modes 2 and 4. In the former case, the transition in buckling mode is smooth and determined by the condition of volume change equality at limit points 1 and 2. In the latter case, the discontinuous transition to mode 4 implies snap-through occurs prior to the maximum pressure with limit point 1 existing at a volume change lower than that of limit point 2.

Another important insight into the snap-through response of imperfect shells can be gained by plotting (Fig. 10 a and b) the snap ratios of both pressure $|p_1 - p_2|/p_1$ and the volume change $|V_1 - V_2|/V_1$, with terms defined in Fig. 7. In these plots the domain of mode 4 is the only domain mapped, since for the others snap-through cannot take place prior to the attainment of the maximum pressure. A reduction of the imperfection amplitude h/l increases the snap ratios $|p_1 - p_2|/p_1$ and $|V_1 - V_2|/V_1$, which translate into the attainment of larger ranges of pressure and volume change. Despite its minor influence, θ_w has an impact on the snap-through response; if θ_w becomes too small, the capacity to snap-through prior to the attainment of the maximum pressure is lost and the shell may enter the domain of mode 1 or mode 2.

To further characterize the competition between limit points 1 and 2 in mode 4, we compare the values of their pressure (Fig. 10c) and volume change (Fig. 10d). The change in the snap-through pressure with respect to reduced values of the defect amplitude h/l and width θ_w is shown in Fig. 10c. Here smaller values make p_1 at limit point 1 approach the maximum pressure p_{\max} at limit point 2, a condition that describes the points on the lower bound of the mode 4 domain. A further decrease of h/l and θ_w make the shell transition to failure mode 2, i.e. the pressure at limit point 1 becomes higher than that of limit point 2 and catastrophic collapse occurs with snap-through. A similar comparison between limit points attributes is shown in Fig. 10d for the volume change. Here, for all combinations of h/l and θ_w in mode 4, the volume change at limit point 1 is well below that at limit point 2 ($V_1/V_{\max} \leq 0.45$), a condition that corresponds to the jump in the maximum volume change V_{\max}/V_0 (Fig. 9b) from mode 2 to mode 4. We also find that the difference in volume change between the limit points reduces with increasing imperfection amplitude h/l and decreasing width θ_w until the point where mode 2 and mode 3 tend to take place at the identical value of volume change. This observation agrees with the discontinuity in V_{\max}/V_0 shown in Fig. 9b, where at the boundary between mode 2 and mode 3 (left-hand side) the discontinuity in V_{\max}/V_0 diminishes for large imperfection amplitude h/l and small width θ_w .

4.2.2. Sensitivity to meridional location of imperfection and radius to thickness ratio of shell

Complementary to the sensitivity plots of the previous section, here we map the role of the other geometric parameters of the imperfect shell, i.e. the defect meridional angle ranging from $\theta_m = 30^\circ$ to 70° , and the radius to thickness ratio ranging from $R/t = 20$ to 150. This time the prescribed quantities are the angular width ($\theta_w = 20^\circ$) and the amplitude ($h/l = 0.2$) of the defect.

Fig. 11a depicts the competition between failure modes for varying values of the meridional angle θ_m and radius to thickness ratio R/t . Since in this case sizeable values of h/l and θ_w are assumed, snap-through buckling occurs at a pressure much lower than the theoretical bifurcation pressure of perfect shells. As a result, the domain of mode 1 recedes in the map, and only failure mode 2 emerges for small θ_m and R/t , with the highest maximum pressure p_{\max}/p_C obtained at point A. The maximum pressure p_{\max}/p_C is attained with limit point 1 and decreases with both the meridional angle θ_m and the radius to thickness ratio R/t . As R/t increases, a switch from failure mode 2 to mode 4 occurs at the boundary of the domains representing the range of R/t values that enable limit point 1 to equal limit point 2. On the other hand, for mode 3 to appear, θ_m should assume large values. For both mode 3 and mode 4, there is a minor change in the maximum pressure for increasing values of R/t and θ_m .

Fig. 11b shows the maximum volume change V_{\max}/V_0 for each buckling mode. Mode 2 features a low maximum volume change, typically below 0.17, meaning that the shell collapses immediately without departing much from its undeformed state. Similar to Fig. 9b, a jump in the maximum volume change is found between mode 2 and mode 4, caused by the difference in volume change between the limit points. For both mode 3 and mode 4, the maximum volume change V_{\max}/V_0 is attained at limit point 2, which decreases monotonically with the meridional angle θ_m but it is insensitive to the radius to thickness ratio R/t . The highest maximum volume change of $V_{\max}/V_0 = 0.52$ appears in mode 4 for a meridional angle at its lower bound ($\theta_m = 30^\circ$).

Similarly to Fig. 10, Fig. 12 depicts the snap-through landscape prior to the attainment of the maximum pressure in mode 4. The snap ratios $|p_1 - p_2|/p_1$ and $|V_1 - V_2|/V_1$ are plotted for varying values of θ_m and R/t , showing the dominant role of the meridional angle θ_m as opposed to that of R/t ; the larger the meridional angle, the smaller the snap ratios. This observation points to the choice of a low meridional angle θ_m to attain more sizable and exploitable variation in pressure and volume change. On the other hand, the radius to thickness ratio R/t has minor influence on the snap ratios, yet a very small R/t is still capable of switching mode 4 into mode 2.

Fig. 12 c and d show the buckling mode competition between the limit points of domain 4. The former is a plot of p_1/p_{\max} , the ratio of the snap-through pressure at limit point 1 over the maximum pressure at limit point 2. The latter is the corresponding plot for V_1/V_{\max} . p_1/p_{\max} increases with the decrease of both the meridional angle and the radius to thickness ratio, with a value close to unity at the boundary between the domains of mode 2 and mode 4. With further decrease in θ_m and R/t , the pressure at limit point 1 overcomes that at limit point 2, hence resembling the conditions of mode 2. In Fig. 12d, the ratio of volume change between the limit points V_1/V_{\max} has a small value from 0.1 to 0.37, a result indicating the large difference between limit points 1 and 2, the former being far below the latter. This explains the abrupt change in the maximum volume change V_{\max}/V_0 observed in Fig. 11b at the boundary between mode 2 and 4. In addition, the value of V_1/V_{\max} increases with θ_m and decreases with R/t , a trend that indicates the occurrence of the limit points at identical values of the volume change, as further corroborated in Fig. 11b for large θ_m and small R/t .

In summary, the sensitivity investigation carried out above provides valuable insights into the competition between the four buckling modes. The snap ratios quantify the variations in pressure and volume change caused by snap-through buckling at limit point 1, while the ratio of snap-through pressure over the maximum pressure and its counterpart in volume change allows to assess the difference in pressure and volume change between limit points 1 and 2. With these metrics it is possible to characterize the four domains. Bifurcation (mode 1) is triggered by small-sized imperfections and provides the highest maximum pressure. However, since an extremely small volume change leads to bifurcation, the collapse is sudden and spontaneous with no warning of departure from the undeformed shape; the shell here exhausts its capacity to provide further resistance to deformation. As the imperfection increases in size, however, the snap-through modes (2, 3, 4) become dominant, thereby providing additional resistance before the attainment of the maximum pressure. Harnessing defect location and size enables to channel the buckling mode and, as needed by the application, the transition between domains,

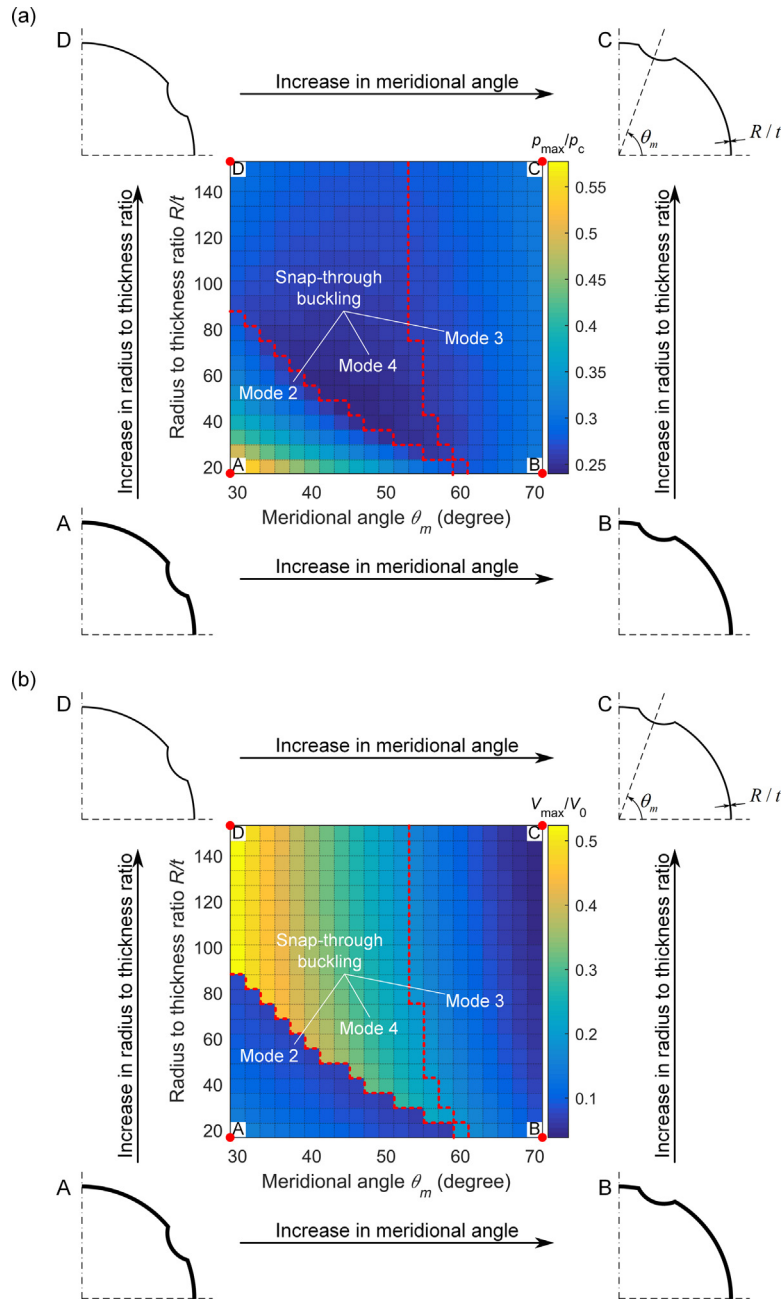


Fig. 11. Role of the meridional angle θ_m and the radius to thickness ratio R/t on (a) the normalized maximum pressure and (b) the normalized volume change at the maximum pressure.

escaping mode 1 to access mode 2 and mode 3, each corresponding to a maximum pressure value attained at either limit point 1 (mode 2), or at limit point 2 (mode 3). Mode 4 combines mode 2 and mode 3 and represents the failure mechanism for which the pressure at limit point 1 is below that of limit point 2.

On the limitations of the sensitivity study here presented, we recall that our numerical analysis can only predict axisymmetric deformations. Peaks of pressure caused by non-axisymmetric modes, such as those in Fig. 6b, cannot be captured, but these peaks should be accounted for, should the application require it. Yet again, the choice of focusing in this sensitivity study on the axisymmetric case rather than the non-axisymmetric one is motivated by the minor discrepancy (3.6%) between their maximum pressure. We also recall that for hemispherical shells, the bifurcation pressure can be significantly 'knocked down' by as-manufactured imperfections, which were not considered here. Their impact on the failure mode, however, would be apparent in the mode 1 domain, which would fill a larger area.

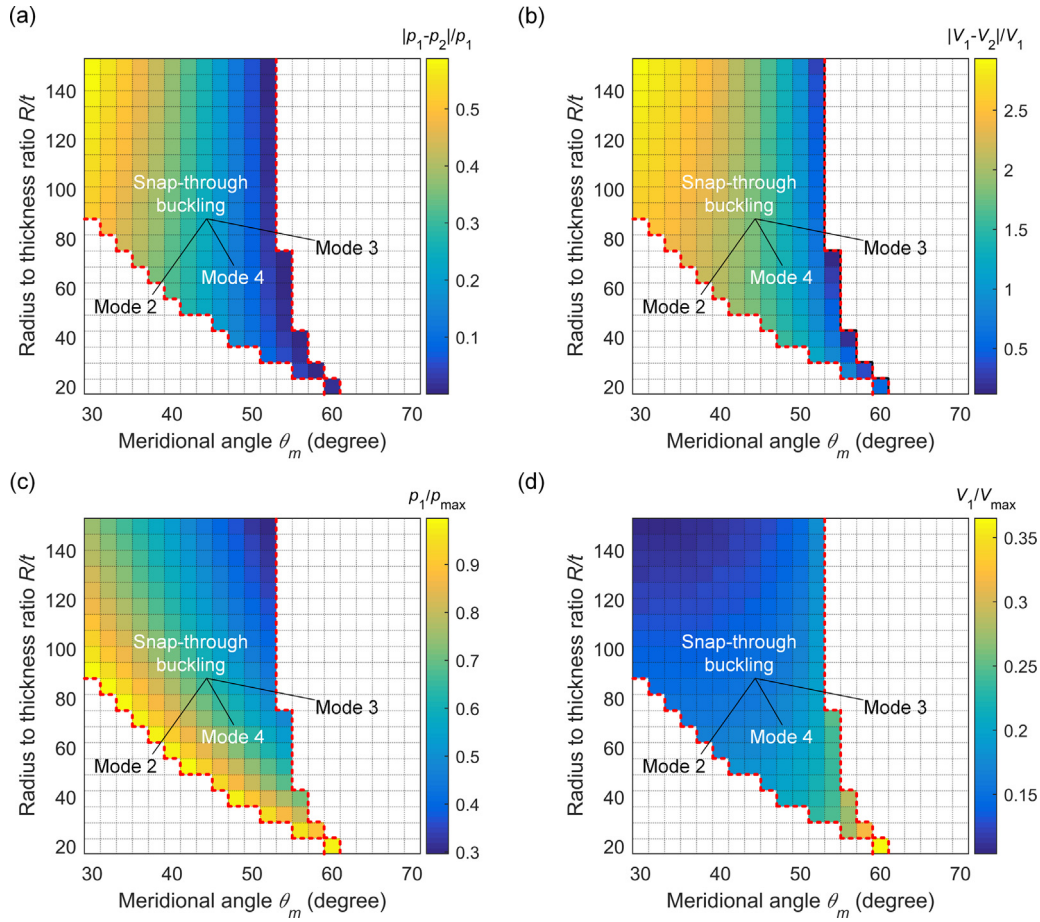


Fig. 12. Role of meridional angle θ_m and radius to thickness ratio R/t on snap-through properties. (a) and (b) Snap ratios of pressure and volume change. (c) Ratio of snap-through pressure over maximum pressure. (d) Ratio of the snap-through volume change over maximum volume change.

5. Concluding remarks

This paper has investigated the impact of a large axisymmetric imperfection on the buckling response of a thin elastic shell subject to uniform external pressure. Our shell theory formulation employs exact stretching and bending strain measures as well as live pressure loading, and can predict buckling for imperfect shells with uniform thickness. For shells of non-uniform thickness, results from experiments and numerical solutions are in quantitative agreement. A number of findings have emerged from the results.

First, a large axisymmetric imperfection can cause the shell response to depart from bifurcation buckling, i.e. the classical dimple-like shape of perfect shells typically triggered by a tiny change in volume. Integrating a large axisymmetric defect into the shell geometry can localize the deformation at the site of the imperfection, which causes snap-through followed by an increase in the post-buckling pressure until the attainment of the maximum pressure. The benefit here is twofold. The maximum achievable volume can reach as high as 0.4, and the maximum attainable pressure is reduced only by 66% from the theoretical buckling pressure of an ideal perfect shell, as opposed to the 90% drop reported in the experimental measurements for as-manufactured perfect shells in the literature.

Second, the buckling response of the imperfect shell can be approximated with an axisymmetric mode. The symmetric breaking of deformation only occurs during the snap-through buckling prior to the attainment of maximum pressure, causing minor (below 4%) deviation in the maximum pressure. This result suggests that the axisymmetric deformation can provide a sufficient level of approximation for shell design.

Third, a sensitivity study on imperfections of varying size and location along with shell radius to thickness ratio has unveiled a number of insights into the buckling landscape of imperfect elastic shells.

- **Buckling modes.** Four modes have been identified for an imperfect shell with axisymmetric defect: bifurcation instability caused by small-sized imperfections, and three snap-through responses yielded by large-sized imperfections. Their domains have been mapped into charts that show their boundaries and buckling mode competition over a range of

combinations of their defect descriptors (defect amplitude h/l , angular width θ_w , and meridional angle θ_m) and shell geometry (radius to thickness ratio R/t);

- **Attainable maximum pressure.** Defect size and location as well as shell radius to thickness ratio can be harnessed to modify the normalized maximum pressure over a large range of values. The bifurcation mode (mode 1), which resembles the response of a perfect shell, yields the highest normalized maximum pressure ranging from $p_{\max}/p_c = 0.78$ to 0.91. The snap-through modes (modes 2, 3, and 4) provide a wide range of maximum pressure from $p_{\max}/p_c = 0.21$ to 0.81. Despite the reduction in maximum pressure, the imperfect shell can still attain values comparable to those measured in literature for as-manufactured perfect shells.
- **Attainable maximum volume change.** Similarly to the maximum pressure, the normalized maximum volume change can also be increased by harnessing the defect geometry and shell radius to thickness ratio. In particular, $\Delta V/V_0$ for mode 1 remains low (2%) and close to the value for a perfect shell (below 1%), whereas for the snap-through modes 2, 3, and 4, V_{\max}/V_0 increases substantially up to 17%, 31%, and 52% respectively.
- **Competition of snap-through buckling modes.** Imperfection amplitude h/l and meridional angle θ_m are the most influential parameters that govern snap-through buckling in mode 4. By harnessing these parameters within the geometric ranges here investigated, the snap ratio of pressure can span the interval from 0 to 0.61, and the snap ratio of volume change can range between 0.12 and 3.35. These ranges offer a sizeable snap-through tunability that could be exploited for the design of soft robots and morphing metamaterials.

Declaration of Competing Interest

The authors declare that they have no known competing financial interests or personal relationships that could have appeared to influence the work reported in this paper.

CRediT authorship contribution statement

Chuan Qiao: Conceptualization, Methodology, Investigation, Validation, Writing - original draft. **Lu Liu:** Methodology, Software. **Damiano Pasini:** Conceptualization, Methodology, Investigation, Supervision, Writing - original draft, Writing - review & editing, Project administration, Funding acquisition.

Acknowledgement

This work was supported by the Natural Sciences and Engineering Research Council of Canada (Grant # 208241).

Appendix A. Approximation of the non-uniform thickness profile of the as-manufactured shell

In Fig. A.1a, we partitioned the thickness profile of the shell into eight sections (i)-(viii) so as to linearly approximate the thickness profile in each section. The acquired data was then used to generate the corresponding FEM model (Fig. A.1b). The nodal thickness profile in the FEM model was expressed using a cylindrical coordinate system (ρ, φ, z) whose origin is located at the center of the spherical shell. As such, the thickness in each of the eight sections is:

$$\begin{aligned} t_i &= 0.25 \\ t_{ii} &= (\rho - 10.15)/2.59 * 0.37 + 0.25 \\ t_{iii} &= -(\rho - 12.74)/1.13 * 0.50 + 0.62 \\ t_{iv} &= 0.25 - (z - 14.51)/5.95 * 0.13 \\ t_v &= (\rho - 16.22)/3.59 * 0.63 + 0.25 \\ t_{vi} &= -(\rho - 19.82)/1.45 * 0.80 + 0.88 \\ t_{vii} &= 0.20 - (z - 11.20)/1.40 * 0.12 \\ t_{viii} &= 0.20 \end{aligned} \quad (A.1)$$

where ρ is the radial distance from the z -axis, φ is the azimuth angle, and z is the height from the plane of equator.

Appendix B. Tensor analysis of the middle surface of a shell

Here we present the main equations of the exact shell theory formulation given by Niordson (1985). With a focus on a shell of an arbitrary shape, the parametric relations f^i between the Cartesian coordinates x^i and the coordinates (u^1, u^2) on the middle surface of the shell can be written as:

$$x^i = f^i(u^1, u^2) \quad (B.1)$$

The first fundamental tensors (metric or fundamental tensor) of the undeformed and the deformed coordinated systems are

$$a_{\alpha\beta} = f_{,\alpha}^i f_{,\beta}^i \quad (B.2)$$

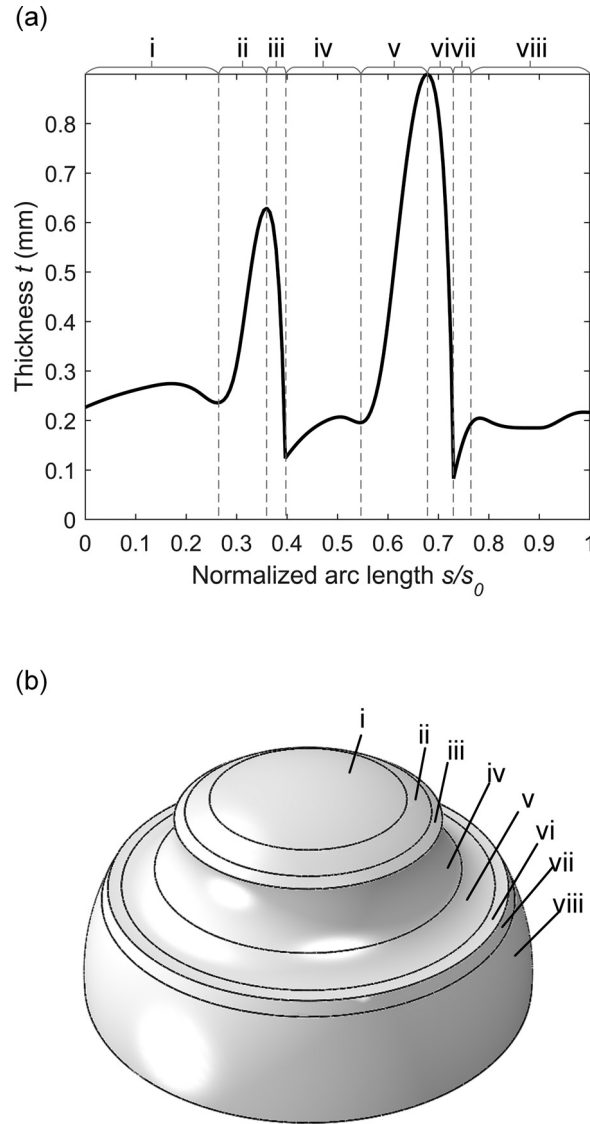


Fig. A.1. Partition of (a) the thickness profile and (b) the FEM model.

and

$$a_{\alpha\beta}^* = (f^i + \bar{v}^i)_{,\alpha} (f^i + \bar{v}^i)_{,\beta} \quad (\text{B.3})$$

where \bar{v}^i is the displacement in the Cartesian coordinates. An asterisk marks quantities in the deformed state. The second fundamental tensors (curvature tensor) of the undeformed and the deformed coordinated systems are

$$d_{\alpha\beta} = X^i f^i_{,\alpha\beta} \quad (\text{B.4})$$

and

$$d_{\alpha\beta}^* = \left(\frac{a}{a^*}\right)^{\frac{1}{2}} \left[\left(1 + p_\varepsilon^\varepsilon + \frac{p}{a}\right) (d_{\alpha\beta} + D_\beta q_\alpha + d_\beta^\gamma p_{\alpha\gamma}) - (q^\rho + \varepsilon^{\rho\beta} \varepsilon^{\gamma\delta} q_\gamma p_{\delta\beta}) (D_\beta p_{\alpha\rho} - d_{\beta\rho} q_\alpha) \right] \quad (\text{B.5})$$

where X^i is a unit vector normal to the middle surface, $p_{\alpha\beta} = D_\alpha v_\beta - d_{\alpha\beta} w$ is the two-dimensional displacement gradient, D_α is the symbol for covariant derivative, $q_\alpha = d_{\alpha\beta} v^\beta + w_{,\alpha}$ is the rotation perpendicular to the normal of the surface, and

$\varepsilon_{\alpha\beta}$ is the alternating tensor. The quantities without indices are given by the determinants:

$$\begin{aligned} a &= \det(a_{\alpha\beta}) = a_{11}a_{22} - a_{12}a_{21} \\ a^* &= \det(a_{\alpha\beta}^*) = a_{11}^*a_{22}^* - a_{12}^*a_{21}^* \\ p &= \det(p_{\alpha\beta}) = p_{11}p_{22} - p_{12}p_{21} \end{aligned} \quad (\text{B.6})$$

The rotation around the normal of the middle surface is

$$\Theta = \frac{1}{2} \varepsilon^{\alpha\beta} p_{\alpha\beta} \quad (\text{B.7})$$

The strain tensor is defined by

$$E_{\alpha\beta} = \frac{1}{2} (a_{\alpha\beta}^* - a_{\alpha\beta}) = \frac{1}{2} (p_{\alpha\beta} + p_{\alpha\beta} + p_{\alpha}^{\lambda} p_{\alpha\lambda} + q_{\alpha} q_{\beta}) \quad (\text{B.8})$$

where the factor $\frac{1}{2}$ is employed to make the definition of strain measure conform with the Lagrangian stretching strain.

The change in curvature is

$$K_{\alpha\beta} = d_{\alpha\beta}^* - d_{\alpha\beta} = \left(\frac{a}{a^*}\right)^{\frac{1}{2}} \left[\left(1 + p_{\varepsilon}^{\varepsilon} + \frac{p}{a}\right) (d_{\alpha\beta} + D_{\beta} q_{\alpha} + d_{\beta}^{\gamma} p_{\alpha\gamma}) - (q^{\rho} + \varepsilon^{\rho\beta} \varepsilon^{\gamma\delta} q_{\gamma} p_{\delta\beta}) (D_{\beta} p_{\alpha\rho} - d_{\beta\rho} q_{\alpha}) \right] - d_{\alpha\beta} \quad (\text{B.9})$$

Since the stretching strains are small in the current study, we assume $a/a^* \approx 1$ in the expression of the curvature change (Eq. (B.9)). This approximation is consistent with previous equations in the literature (Hutchinson (2016)).

According to Koiter and van der Heijden (2009), the volume change is

$$\Delta V = \int_S \left\{ w + \frac{1}{2} (w p_{\alpha}^{\alpha} - q_{\alpha} u^{\alpha}) + \frac{1}{6} [w (p_{\alpha}^{\alpha} p_{\beta}^{\beta} - p_{\alpha}^{\beta} p_{\alpha}^{\beta}) - 2u^{\alpha} (q_{\beta} p_{\alpha}^{\beta} - q_{\alpha} p_{\beta}^{\beta})] \right\} dS \quad (\text{B.10})$$

Appendix C. Solution method for axisymmetric deformations with the shell formulation

We solved the axisymmetric problem of the imperfect shell based on the shell formulation in Section 3.2 with a numerical method (Hutchinson (2016)). The hemispherical shell with as-designed large imperfection is divided into three parts: the imperfection, and the parts above and below the imperfection. These parts are connected by imposing the following continuity condition on displacement and rotation for axisymmetric deformation:

$$\begin{aligned} u_1^+ &= u_1^- \\ u_2^+ &= u_2^- \\ \varphi_{\theta}^+ &= \varphi_{\theta}^- \end{aligned} \quad (\text{C.1})$$

where u_1 is the displacement along the horizontal direction, u_2 is the displacement along the vertical direction, φ_{θ} is the rotation, and the signs + and - indicate the two sides at a boundary.

Within each domain, the shell is discretized into N sections of equal length. We assign displacements tangent and normal to the middle surface, u_{θ} and w , as $6N + 6$ unknowns to the nodes. An additional unknown is the external pressure p . The $6N + 7$ unknowns form a vector λ of unknown displacements and pressure. Within each section, we use the shell theory for axisymmetric deformations presented in Section 3.2 to calculate the average of the potential energy density. Then, the total potential energy is obtained by integrating the potential energy density in each section. The integrations and derivatives are computed numerically.

The solution is steered with the pole displacement w_{pole} . For each step, we prescribe the displacement at the upper pole w_{pole} . Then, we update the increment of the vector of unknowns $\Delta\lambda$ with Newton iterations to find a new equilibrium state

$$\Delta\lambda = -H^{-1}G \quad (\text{C.2})$$

where G is the gradient of the total potential energy, and H^{-1} is the inverse of the hessian matrix. For each step, the Newton iteration is repeated until the solution converges. While this method is straightforward to code as mentioned by Hutchinson (2016), it posed a limitation. When the number of unknowns is large, the computation of the hessian and its inverse becomes too expensive and reaching convergence in the process of finding a solution might be challenging.

Appendix D. Convergence study for theoretical and FEM models

We first performed a set of convergence studies for both the axisymmetric solution based on the shell formulation and the FEM simulations. The geometry parameters of the shell for both cases are listed in Table 1 (Section 3.1.1). The convergence study is performed by assuming a uniform thickness profile with a radius to thickness ratio $R/t = 123.6$.

Fig. D.1 shows the convergence study for the axisymmetric solution based on shell theory. By increasing the number of nodes, the solution gradually approaches the curve of the FEM simulation for axisymmetric deformations. The results of

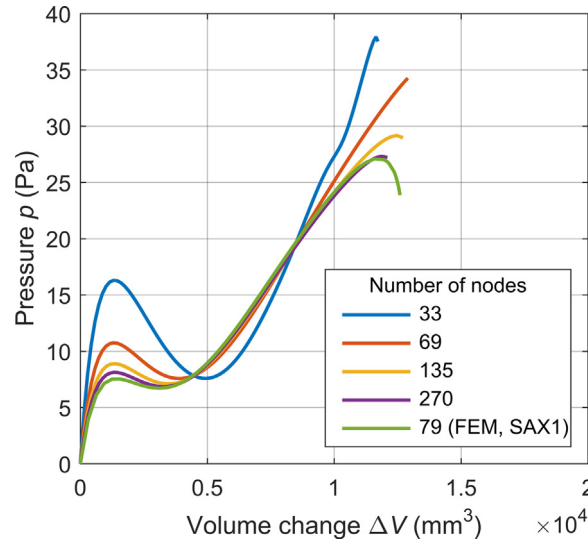


Fig. D.1. Convergence study of the axisymmetric solution based on shell theory. The green curve with SAX1 elements for axisymmetric deformation is shown as a reference.

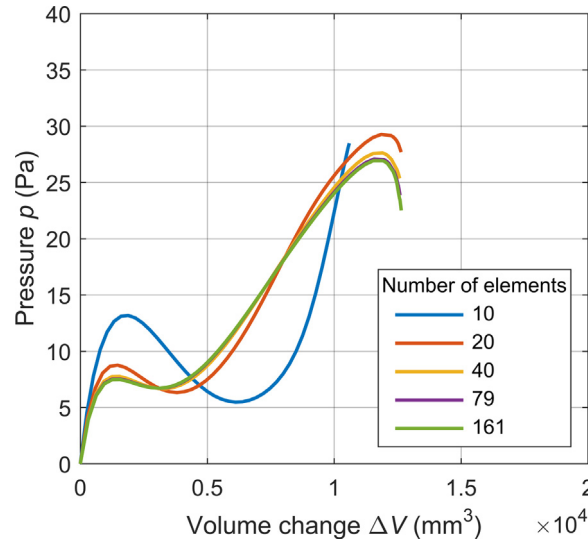


Fig. D.2. Convergence study of FEM simulations with SAX1 axisymmetric line elements

shell theory match well with the FEM results when 270 nodes are used in the numerical solution. Any further increase in the number of nodes makes the solution difficult to converge. Thus in this work, we use 270 nodes.

Fig. D.2 shows the results for FEM simulations with SAX1 axisymmetric line elements. The simulation with 79 elements converges to the simulation employing 161 elements. Hence in this work we select an average of 80 elements.

Fig. D.3 shows the results of the convergence study for FEM simulations with S4R and S3R shell elements. The simulation result with 10288 elements converges to that with 15220 elements. Hence in this work, we use around 10000 elements for the FEM simulations with shell elements.

Appendix E. The role of clamped support on the development of mode 4

Here we aim at understanding the role of clamping the shell equator to trigger mode 4, i.e. snap-through buckling combining mode 2 and 3. A set of axisymmetric simulations have been performed to compare the buckling responses of two cases: a full sphere and a hemispherical shell, both with a prescribed imperfection. Fig. E.1 (below) shows the results. As observed, their normalized pressure curves and shell deformations show no difference for almost the entire response (stages (i) to (iii)), indicating that the influence of the clamping at the equator is not sizeable for shell buckling. This shows that mode 4 does appear also for the full sphere and it is not caused by clamping the equator. The difference between a full

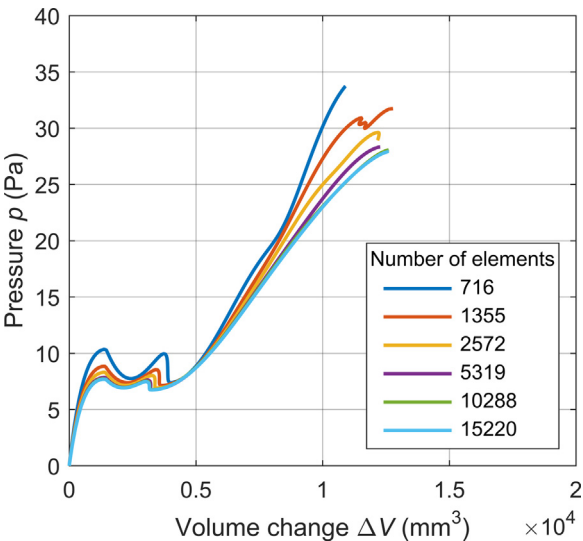


Fig. D.3. Convergence study of FEM simulations with S4R and S3R shell elements

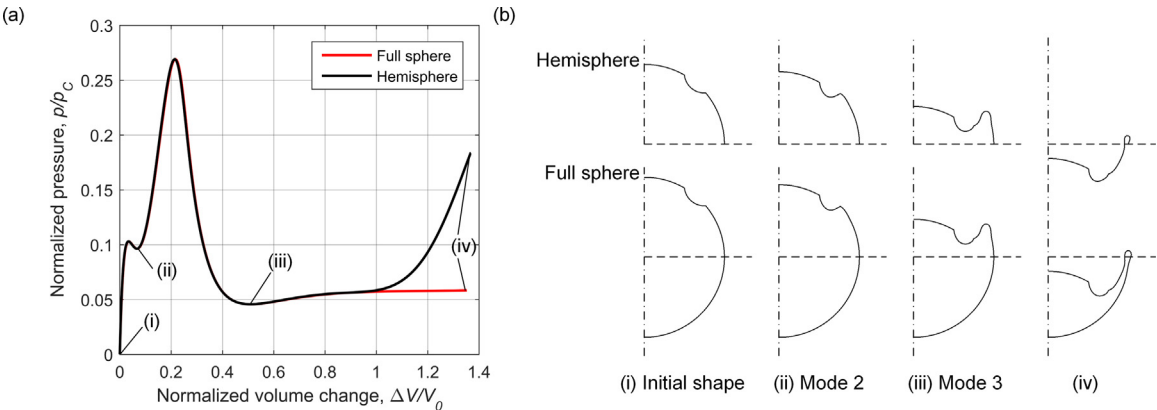


Fig. E.1. Responses of full and hemispherical shells with prescribed imperfection ($h/l = 0.2$, $\theta_w = 20^\circ$, $R/t = 124$, and $\theta_m = 50^\circ$). (a) Pressure versus change in volume normalized by the negative of the volume within the middle surface of the undeformed hemisphere, $V_0 = -2\pi R^3/3$. (b) Cross-section view of deformed modes (mode 4).

sphere and a hemisphere becomes significant only when the deformation zone reaches the equator (stage (iv)), an instance that shows that clamping the equator does constrain shell deformation. At this stage, collapse appears as shell eversion, a condition not examined in this work.

Appendix F. Cascade of snap through buckling in a shell with multiple imperfections

A cascade of snap through buckling can occur for certain combinations of defects. Fig. F.1 shows an example where two imperfections are examined in a shell with radius of 25 mm and radius to thickness ratio of 124 (Table F.1 lists the geometric parameters). The result shows that the shell undergoes twice snap-through buckling with mode 2, before attaining the maximum pressure with mode 3 (Table R.1).

Table. R.1			
Geometric parameters of the imperfections.			
	h/t	$\theta_w(^{\circ})$	$\theta_m(^{\circ})$
Upper imperfection	0.21	15	47
Lower imperfection	0.26	15	24

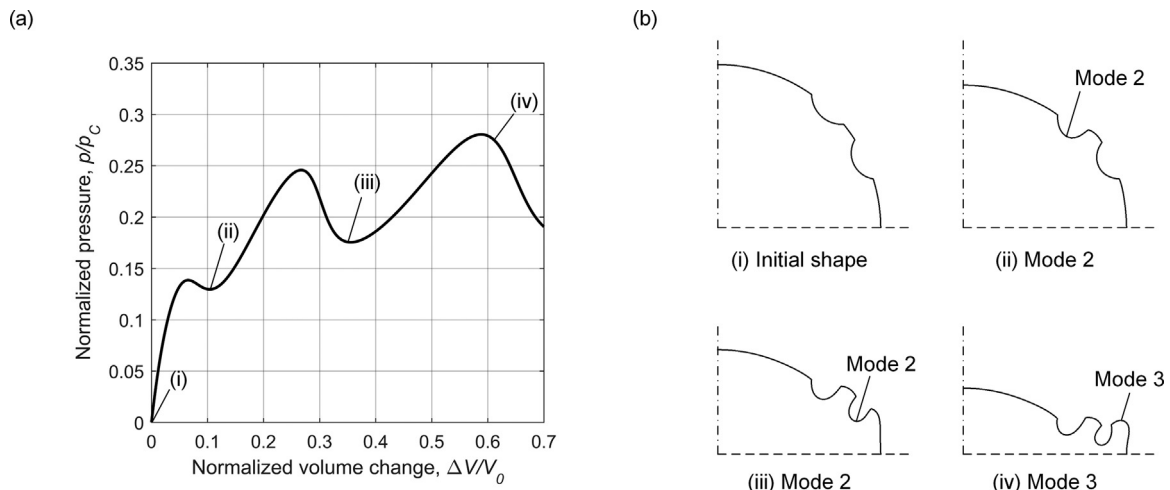


Fig. F.1. Responses of shell with two imperfections. (a) Pressure versus change in volume normalized by the negative of the volume within the middle surface of the undeformed hemisphere, $V_0 = -2\pi R^3/3$. (b) Cross-section view of deformed modes (mode 4).

References

- Arfsten, J., Leupold, S., Bradtmöller, C., Kampen, I., Kwade, A., 2010. Atomic force microscopy studies on the nanomechanical properties of *Saccharomyces cerevisiae*. *Colloid Surf. B-Biointerfaces* 79 (1), 284–290.
- Audoly, B., Hutchinson, J.W., 2019. Localization in spherical shell buckling. *J. Mech. Phys. Solids* doi:10.1016/j.jmps.2019.103720.
- Bende, N.P., Evans, A.A., Innes-Gold, S., Marin, L.A., Cohen, I., Hayward, R.C., Santangelo, C.D., 2015. Geometrically controlled snapping transitions in shells with curved creases. *Proc. Natl. Acad. Sci.* 112 (36), 11175–11180.
- Blachut, J., 2015. Locally flattened or dented domes under external pressure. *Thin-Walled Struct.* 97, 44–52.
- Blachut, J., 2016. Buckling of composite domes with localised imperfections and subjected to external pressure. *Compos. Struct.* 153, 746–754.
- Blachut, J., Galletly, G.D., 1993. Influence of local imperfections on the collapse strength of domed end closures. *Proc. Inst. Mech. Eng. Part C-J. Eng. Mech. Eng. Sci.* 207 (3), 197–207.
- Blachut, J., Magnucki, K., 2008. Strength, stability, and optimization of pressure vessels: review of selected problems. *Appl. Mech. Rev.* 61 (6) 060801-060801-060833.
- Budiansky, B., 1968. Notes on nonlinear shell theory. *J. Appl. Mech.-Trans. ASME* 35 (2), 393–401.
- Bushnell, D., 2014. Shell buckling.
- Carlson, R.L., Sendelbeck, R.L., Hoff, N.J., 1967. Experimental studies of the buckling of complete spherical shells. *Exp. Mech.* 7 (7), 281–288.
- Donnell, L.H., 1934. A new theory for the buckling of thin cylinders under axial compression and bending. *Aeronaut. Eng.-Trans. ASME* 56 (11), 795–806.
- Donnell, L.H., Wan, C.C., 1950. Effect of imperfections on buckling of thin cylinders and columns. *J. Appl. Mech.-Trans. ASME* 17, 73–83.
- Evkin, A.Y., Lykhachova, O.V., 2017. Energy barrier as a criterion for stability estimation of spherical shell under uniform external pressure. *Int. J. Solids Struct.* 118–119, 14–23.
- Fan, Q.S., 1989. Post-buckling behaviour and imperfection sensitivity of spherical shells based on nonlinear elastic stability theory. *Thin-Walled Struct.* 8 (1), 1–18.
- Gomez, M., Moulton, D.E., Vella, D., 2019. Dynamics of viscoelastic snap-through. *J. Mech. Phys. Solids* 124, 781–813.
- Homewood, R.H., Brine, A.C., Johnson, A.E., 1961. Experimental investigation of the buckling instability of monocoque shells. *Exp. Mech.* 1 (3), 88–96.
- Hutchinson, J.W., 2016. Buckling of spherical shells revisited. *Proc. R. Soc. A-Math. Phys. Eng. Sci.* 472 (2195), 20160577.
- Hutchinson, J.W., Koiter, W.T., 1970. Postbuckling theory. *Appl. Mech. Rev.* 23, 1353–1366.
- Jose, J., Kamp, M., van Blaaderen, A., Imhof, A., 2014. Unloading and reloading colloidal microcapsules with apolar solutions by controlled and reversible buckling. *Langmuir* 30 (9), 2385–2393.
- Kao, R., 1972. A note on buckling of spherical caps with initial asymmetric imperfections. *J. Appl. Mech.-Trans. ASME* 39 (3), 842–844.
- Kao, R., Perrone, N., 1971. Asymmetric buckling of spherical caps with asymmetrical imperfections. *J. Appl. Mech.-Trans. ASME* 38 (1), 172–178.
- Kaplan, A., Fung, Y., 1954. A Nonlinear Theory of Bending and Buckling of Thin Elastic Shallow Spherical Shells. National Advisory Committee for Aeronautics, Washington, DC Technical Note 3212.
- Katifori, E., Alben, S., Cerda, E., Nelson, D.R., Dumais, J., 2010. Foldable structures and the natural design of pollen grains. *Proc. Natl. Acad. Sci.* 107 (17), 7635–7639.
- Koga, T., Hoff, N.J., 1969. The axisymmetric buckling of initially imperfect complete spherical shells. *Int. J. Solids Struct.* 5 (7), 679–697.
- Koiter, W.T., 1945. On the stability of elastic equilibrium. Polytechnic Institute of Delft, Delft, The Netherlands. (An English translation is available as NASA Tech. Trans. F 10833, 1967.)
- Koiter, W.T., 1966. On the nonlinear theory of thin elastic shells. *Proc. K. Ned. Akad. Wet. B* 69, 1–54.
- Koiter, W.T., 1967. General equations of elastic stability for thin shells. In: *Proceedings, Symposium on the Theory of Shells to Honor Lloyd Hamilton Donnett*, pp. 157–230.
- Koiter, W.T., van der Heijden, A.M.A., 2009. *W.T. Koiter's Elastic Stability of Solids and Structures*. Cambridge University Press, Cambridge.
- Krenke, M.A., Kiernan, T.J., 1963. Elastic stability of near-perfect shallow spherical shells. *AIAA J.* 1 (12), 2855–2857.
- Lee, A., Brun, P.T., Marthelot, J., Balestra, G., Gallaire, F., Reis, P.M., 2016a. Fabrication of slender elastic shells by the coating of curved surfaces. *Nat. Commun.* 7, 11155.
- Lee, A., López Jiménez, F., Marthelot, J., Hutchinson, J.W., Reis, P.M., 2016b. The geometric role of precisely engineered imperfections on the critical buckling load of spherical elastic shells. *J. Appl. Mech.-Trans. ASME* 83 (11) 111005-111005-111011.
- NASA, 1969. Buckling of thin-walled doubly curved shells. NASA Space Veh. Des. Criteria NASA SP-8032.
- Nguyen, X.T., Hou, S., Liu, T., Han, X., 2016. A potential natural energy absorption material – Coconut mesocarp: Part A: Experimental investigations on mechanical properties. *Int. J. Mech. Sci.* 115–116, 564–573.
- Niordson, F.I., 1985. *Shell theory*. Elsevier Science Pub. Co., New York.
- Pan, B.B., Cui, W.C., Shen, Y.S., 2012. Experimental verification of the new ultimate strength equation of spherical pressure hulls. *Mar. Struct.* 29 (1), 169–176.

- Pan, B.B., Cui, W.C., Shen, Y.S., Liu, T., 2010. Further study on the ultimate strength analysis of spherical pressure hulls. *Mar. Struct.* 23 (4), 444–461.
- Paulose, J., Nelson, D.R., 2013. Buckling pathways in spherical shells with soft spots. *Soft Matter*. 9 (34), 8227–8245.
- Pezzulla, M., Shillig, S.A., Nardinocchi, P., Holmes, D.P., 2015. Morphing of geometric composites via residual swelling. *Soft Matter*. 11 (29), 5812–5820.
- Riks, E., 1979. An incremental approach to the solution of snapping and buckling problems. *Int. J. Solids Struct.* 15 (7), 529–551.
- Sanders, J.L., 1963. Nonlinear theories for thin shells. *Q. Appl. Math.* 21 (1), 21–36.
- Seaman, L., 1962. The nature of buckling in thin spherical shells. watertown arsenal labs MA.
- Taffetani, M., Jiang, X., Holmes, D.P., Vella, D., 2018. Static bistability of spherical caps. *Proc. R. Soc. A-Math. Phys. Eng. Sci.* 474 (2213), 20170910.
- Thompson, J.M.T., Heijden, G.H.M.v.d., 2014. Quantified "shock-sensitivity" above the Maxwell load. *Int. J. Bifurcation Chaos* 24 (03), 1430009.
- Tsien, H.-S., 1942. A theory for the buckling of thin shells. *J. Aeronaut. Sci.* 9 (10), 373–384.
- Vaziri, A., Mahadevan, L., 2008. Localized and extended deformations of elastic shells. *Proc. Natl. Acad. Sci.* 105 (23), 7913–7918.
- Vieira, J., Osório, J.M.A., Mouta, S., Delgado, P., Portinha, A., Meireles, J.F., Santos, J.A., 2017. Kansei engineering as a tool for the design of in-vehicle rubber keypads. *Appl. Ergon.* 61, 1–11.
- von Kármán, T., Tsien, H.-S., 1939. The buckling of spherical shells by external pressure. *J. Aeronaut. Sci.* 7 (2), 43–50.
- von Kármán, T., Tsien, H.-S., 1941. The buckling of thin cylindrical shells under axial compression. *J. Aeronaut. Sci.* 8 (8), 303–312.
- Wagner, H.N.R., Hühne, C., Niemann, S., 2018. Robust knockdown factors for the design of spherical shells under external pressure: Development and validation. *Int. J. Mech. Sci.* 141, 58–77.
- Zoelly, R., 1915. Ueber ein knickungsproblem an der kugelschale. ETH Zurich, Zurich, Switzerland Ph.D. thesis.